X-ray response of CdZnTe detectors grown by the vertical Bridgman technique: energy, temperature and high flux effects

L. Abbene[a*], G. Gerardi[a], A. A. Turturici[a], G. Raso[a], G. Benassi[b], M. Bettelli[c], N. Zambelli[b], A. Zappettini[c] and F. Principato[a]

[a]*Dipartimento di Fisica e Chimica (DiFC), Università di Palermo, Viale delle Scienze, Edificio 18, Palermo 90128, Italy*

[b]*due2lab s.r.l., Via Paolo Borsellino 2, Scandiano, Reggio Emilia, 42019, Italy*

[c]*IMEM/CNR, Parco Area delle Scienze 37/A, Parma 43100, Italy.*

Abstract

Nowadays, CdZnTe (CZT) is one of the most key materials for the development of room temperature X-ray and gamma ray detectors and great efforts have been made on both the device and the crystal growth technologies. In this work, we present the results of spectroscopic investigations on new boron oxide encapsulated vertical Bridgman (B-VB) grown CZT detectors, recently developed at IMEM-CNR Parma, Italy. Several detectors, with the same electrode layout (gold electroless contacts) and different thicknesses (1 and 2.5 mm), were realized: the anode is a central electrode (2 x 2 mm^2) surrounded by a guard-ring electrode, while the cathode is a planar

---

[*] Corresponding author. Dipartimento di Fisica e Chimica, Università di Palermo, Viale delle Scienze, Edificio 18, Palermo 90128, Italy. Tel.: +39-091-23899081; fax: +39-091-23860815;
e-mail address: leonardo.abbene@unipa.it (L. Abbene)

electrode covering the detector surface (4.1 x 4.1 mm^2). The detectors are characterized by electron mobility-lifetime product ($\mu_e \tau_e$) values ranging between 0.6 and $1 \cdot 10^{-3}$ cm^2/V and by low leakage currents at room temperature and at high bias voltages (38 nA/cm^2 at 10000 V/cm). The spectroscopic response of the detectors to monochromatic X-ray and gamma ray sources (^{109}Cd, ^{241}Am and ^{57}Co), at different temperatures and fluxes (up to 1 Mcps), was measured taking into account the mitigation of the effects of incomplete charge collection, pile-up and high flux radiation induced polarization phenomena. A custom-designed digital readout electronics, developed at DiFC of University of Palermo (Italy), able to perform a fine pulse shape and height analysis even at high fluxes, was used. At low rates and at room temperature, the detectors exhibit an energy resolution FWHM around 4 % at 59.5 keV, for comparison an energy resolution of 3% was measured with Al/CdTe/Pt detectors by using the same electronics; while, at 750 kcps, energy resolution values of 7 % and 9 % were measured, with throughputs of 2 % and 60 % respectively. No radiation polarization phenomena were observed at room temperature up to 1 Mcps (^{241}Am source, 60 keV), while a detector collapse characterizes the samples at T<10 °C.

Comparison with the traveling heater method (THM) grown CZT detectors (REDLEN, Canada), fabricated with the same electrode layout, was also presented.

These activities are in the framework of an Italian research project on the development of energy-resolved photon counting (ERPC) systems for high flux energy-resolved X-ray imaging.

Keywords

CdZnTe detectors; boron oxide encapsulated vertical Bridgman; X-ray and gamma ray detectors; high flux; digital pulse shape analysis; energy-resolved photon counting detectors.

1. Introduction

In the last two decades, cadmium telluride (CdTe) and cadmium zinc telluride (CdZnTe or CZT) detectors are widely developed and used for room temperature X-ray and gamma ray spectroscopy [1-4]. CZT/CdTe detectors with thicknesses of 2–3 mm are able to efficiently absorb X rays in the 1–140 keV range and to provide good energy resolution even at room temperature. Recently, CdTe/CZT detectors, with pixelated electrode structures, were proposed for the development of energy-resolved photon counting (ERPC) systems for high flux energy-resolved X-ray imaging, very appealing in diagnostic medicine, industrial imaging and security screening [5-11].

Due to the high-flux conditions of these applications ($>10^6$ photons mm^{-2} s^{-1}), detectors with high bias voltage operation and good charge transport properties are required. Typically, CZT detectors with quasi-ohmic contacts (Au/CZT/Au, Pt/CZT/Pt) [6,12,13] compete with CdTe detectors with rectifying contacts (In/CdTe/Pt, Al/CdTe/Pt) [1,4,9,14], taking into account *bias induced polarization* [15-17] and *high flux radiation induced polarization* phenomena [18-19]. CdTe detectors with rectifying contacts, despite the excellent room temperature performance, suffer from the bias induced polarization [15-17]: a space charge builds up with time under the rectifying contact (anode electrode) producing time-changes in the electric field profile [17] and then spectroscopic degradations. This limited the thickness of the CdTe detectors (typically < 2 mm) and the working operation at low temperatures. CZT detectors with quasi-ohmic contacts are immune to the bias induced polarization, allowing the fabrication of thicker devices (> 2 mm) and room temperature operation. High flux radiation induced polarization is the major drawback of CZT detectors for ERPC systems. As well documented in the literature [7,18-19], high fluxes produce a charge buildup within the detector, which collapses the electric field and results in a catastrophic reduction of the charge collection efficiency. Due to the dependence of this effect on the charge transport properties of the crystal (mainly on the hole mobility-lifetime product), the bias voltage and the temperature, a careful choice of the detector material, the device properties (electrode contact, bias voltage, thickness) and the operating temperature is essential for the development of high-flux ERPC systems.

Recently, within an Italian research collaboration (DiFC of University of Palermo and IMEM-CNR Parma), we proposed to develop ERPC prototypes, based on CZT pixel detectors and digital pulse processing (DPP) electronics, for high flux energy resolved X-ray imaging applications (1-140 keV). In this framework, we developed, at first step, some CZT prototypes, with planar electrode structures, to investigate on both the crystal and the device properties. In this work, we will present the results of spectroscopic investigations (X-ray response at both low and high fluxes, charge transport properties, temperature dependence and spectral improvements through digital pulse shape analysis) on boron oxide encapsulated vertical Bridgman (B-VB) grown CZT detectors, recently developed at IMEM-CNR Parma, Italy [3, 20-24]. A fine characterization of the response of the detectors, at both low (< 300 cps) and high (up to 1 Mcps) rates, to monochromatic X-ray and gamma ray sources (^{109}Cd, ^{241}Am and ^{57}Co) was performed by using a custom-designed digital readout electronics, developed at DiFC of University of Palermo (Italy) [25-27]. The readout electronics is able to continuously digitize and process the signals from the detectors (i.e. the preamplifier output signals) and performs a fine pulse shape and height analysis even at high fluxes. A comparison with the traveling heater method (THM) grown CZT detectors (REDLEN, Canada), fabricated with the same electrode layout was also presented.

2. Materials and methods

2.1. Detectors

The detectors are based on CZT crystals (4.1 x 4.1 x 1, 2.5 mm^3), grown by the Boron oxide encapsulated Vertical Bridgman (B-VB) technique, which are currently produced at IMEM-CNR (Parma, Italy) [3, 20-24]. Further CZT samples (4.1 x 4.1 x 1, 3 mm^3) were also fabricated by using CZT crystals grown by REDLEN Technologies (Canada) with the Traveling Heater Method (THM) technique [12, 13, 25]. Gold electroless contacts were realized by due2lab s.r.l and IMEM-CNR on both the anode (prepared by using water solutions) and the cathode (prepared by alcoholic solutions) of all CZT samples (B-VB and THM crystals). The anode surface is characterized, for all detectors, by a central electrode (2 x 2 mm^2) surrounded by a guard-ring electrode (Fig. 1). The width of the guard-ring is 950 μm and the gap between the electrodes is 50 μm. The cathode is a planar electrode covering the detector surface. The main characteristics of the samples are summarized in Table 1.

To amplify and filter the detector signals, we used a commercial AC-coupled charge sensitive preamplifier CSP (A250, Amptek, USA) with a nominal ENC of about 1 keV.

2.2. Digital readout electronics

The response of the detectors at both low and high fluxes was measured by using a custom digital readout electronics, developed at DiFC of University of Palermo (Italy) [26-28]. In this section, we will present a brief description of the digital pulse processing (DPP) system. A detailed description of the system is reported in previous works [26-28].

The DPP system, by digitizing and processing the output waveform from radiation detectors (i.e. the output CSP waveform), is able to perform multi-parameter analysis (arrival time, pulse width, pulse height, pulse peaking time, etc.) even at high input counting rates (*ICRs*). The DPP system consists of four digitizers (16 channels) and a PC, which controls all digitizing functions, the acquisition and the analysis. We used commercial digitizers (DT5724, CAEN S.p.A., Italy) (www.caentechnologies.com), each housing four high speed ADCs (16 bit, 100 MS/s). The PC runs a C++ program able to control (via optical or USB link) all digitizer functions, to acquire packed data and to produce the results.

The pulse processing analysis is performed by using a custom DPP firmware uploaded to the digitizers. The DPP firmware was developed by our group and successfully used for both off-line and on-line analysis [29-33].

A general overview of the method is presented below (Fig. 2). The DPP method is based on two pipelined shaping steps: a *fast* and a *slow* shaping. The CSP output waveform is shaped by using the classical single delay line (SDL) shaping technique [34]. SDL shaping is obtained by subtracting from the original pulse its delayed and attenuated fraction. SDL shaping gives short rectangular output pulses with fast rise and fall times. Generally, two main features characterize the SDL shaping: (i) the time width of each SDL shaped pulse is well defined (delay time+CSP peaking time) and (ii) if the delay time is greater than the peaking time of the CSP pulse, the SDL shaping also preserves the leading edge (pulse height and peaking time) of each CSP output pulse. These features make SDL shaping very appealing for timing and *PSHA* (pulse shape and height analysis) at both low and high ICRs.

Through the *fast SDL shaping* the following operations are performed:

(i) pulse detection and time-tag triggering,

(ii) fast pulse shape and height analysis (fast PSHA), that provides energy spectra with high throughputs (i.e. the OCR/ICR, where OCR is the output counting rate); the fast PSHA is performed on the SDL pulses by using a short delay time (near to the CSP peaking time) and a fast baseline recovery by using a running average value of a fixed number of samples preceding the SDL pulse, where no further pulses are present; due to the short delay time, used to ensure high throughputs, the energy resolution of energy spectra is generally poorer than the resolution of the spectra obtained from the slow PSHA; the time width (the pulse shape) of the SDL shaped pulses is also measured;

(iii) pile-up rejection (PUR) for the slow analysis; The PUR is used to select time windows of the CSP waveform for the slow PSHA. Each selected time window of the CSP waveform is termed *Snapshot,* while the width of this window, user-chosen, is termed *Snapshot Time (ST).* If two detected fast SDL pulses are within *ST/2* of each other, then neither pulse will be selected; i.e. a pulse is accepted if it is not preceded and not followed by another pulse in the ST/2 time window periods.

The main feature of the *slow SDL shaping* is that the pulse height and shape analysis (PSHA) is performed on each PUR selected *Snapshot*, containing only one CSP pulse. The pulse height analysis is performed by applying a SDL shaping with a delay time longer than pulse peaking time, an automatic baseline restoration and an optimized low-pass filter (trapezoidal filter) to all the samples of each slow SDL shaped pulse. The energy resolution strongly depends on the *ST* values; as the shaping time of classic analog systems, long *ST* values give better energy resolution. Through the *slow* SDL shaping, the system is able to provide, for each selected CSP pulse, the following results:

(i) trigger time,

(ii) pulse height

(iii) peaking time.

The shape of the pulses (the *peaking time* of the slow SDL shaped pulses and the *time width* of the fast SDL shaped pulses) and its correlation with the pulse height is very helpful to improve the detector performance. Pulse shape discrimination (*PSD*) techniques were successfully used in our previous works [10, 28, 31] to minimize incomplete charge collection effects, pile-up and charge sharing.

Both the time width of the pulses from the fast shaping and the *ST* are dead times for the system with a well defined modeling (paralyzable dead time) [27]. In particular, the fast analysis is characterized by a dead time (*fast dead time*) equal to the mean value of the time widths of the fast shaped pulses; while, the dead time of the slow analysis is equal to *ST – fast dead time* [27].

As well highlighted in a previous work [27], the true ICR can be estimated or from an exponential best fit of the measured time-interval distribution (TID) of the fast SDL pulses, or by applying the inversion of the throughput formula of the fast analysis.

2.3. Experimental procedures

The electrical properties (current-voltage curves) of the detectors were measured by using a high voltage source meter Keithley 2410, which provides the detector bias voltage, and the source-measure unit Keithley 236 configured as electrometer. The guard ring of the detectors is held at zero potential to prevent surface leakage currents.

To investigate on the spectroscopic performance of the detectors, we used X-ray and gamma ray calibration sources (^{109}Cd: 22.1, 24.9 and 88.1 keV; ^{241}Am: 59.5, 26.3 keV; ^{57}Co: 122.1, 136.5 keV and the W fluorescent lines, $K_{\alpha1}$=59.3 keV, $K_{\alpha2}$=58.0 keV, $K_{\beta1}$=67.1 keV, $K_{\beta3}$=66.9 keV, produced in the source backing). We used two different ^{241}Am sources: (i) a low- activity source (0.1 MBq) also emitting the Np L X-ray lines (13-21 keV) and (ii) a high-activity source (370 MBq) where the Np L X-ray lines are shielded by the source holder. The 14 keV gamma line of the ^{57}Co source is also shielded by the source holder. To obtain different input counting rates (ICRs) of the impinging photons on the detector (through the cathode surface), we changed the irradiated area of the detector using collimators with different geometries.

The detector and the charge sensitive preamplifiers (CSPs) were enclosed in a shielded box placed on a Peltier thermal stage with temperature control within 0.1°C, and filled with nitrogen gas to prevent condensation. The detector was irradiated through a light-tight beryllium window.

3. Measurements and Results

In this section we will present the results of a full characterization (electrical, charge transport and spectroscopic properties) of the CZT detectors at room and low temperatures, low and high rates. The spectroscopic response of the detectors will be measured, taking into account the mitigation of incomplete charge collection and pile-up effects, through the digital pulse shape analysis (peaking time of the slow SDL shaped pulses and the time width of the fast SDL shaped pulses). Particular attention will be given to the high flux radiation induced polarization effects on the detectors.

Moreover, a comparison between the thin CZT detectors (1 mm thick) and an Al/CdTe/Pt detector, characterized by the same geometrical electrode layout and similar thickness (0.75 mm thick), will be also presented. The CdTe detector with rectifying contacts was fabricated by Acrorad (Japan) and both the electrical [16, 35] and spectroscopic [28, 36] properties have been already investigated in previous works.

3.1. Electrical and charge transport properties

Fig. 3 shows the current-voltage (*I-V*) characteristics of the IMEM 3 CZT detector (1 mm thick) at T = 25 °C and T = 15 °C. The behaviour of the I-V curves is typical of the Au/CZT/Au contacts, i.e. of a metal–semiconductor–metal (MSM) device with two back-to-back Schottky barriers [37,38]. As clearly visible in the figure, the IMEM 3 detector is characterized by very low leakage currents in the reverse bias region: 3.5 nA/cm^2 at 1000 V/cm at T = 25 °C (1.2 nA/cm^2 at T = 15°C); typically, Au/CZT/Au detectors (fabricated by REDLEN) are characterized by leakage currents ranging from 50 nA/cm^2 to 500 nA/cm^2 at 1000 V/cm [12-13]. Moreover, the detector ensures a low leakage current of 38 nA/cm^2 (T = 25°C) even at very high electric field of 10000 V/cm.

Fig. 4 shows an interesting comparison among the *I–V* curves, under reverse bias voltage operation, of the 1 mm CZT detectors (B-VB and THM) and the Al/CdTe/Pt detector. Concerning the CZT detectors, the THM grown detectors are characterized by leakage current values (e.g. 13 nA/cm^2 at 1000 V/cm for REDLEN 2.1) in perfect agreement with the literature (from 50 nA/cm^2 to 500 nA/cm^2 at 1000 V/cm) [12-13]. Despite both B-VB and THM grown CZT samples were fabricated with the same electrode deposition technique and they are characterized by similar crystal resistivity values (~2x10^{10} Ω·cm), the THM grown CZT samples always showed higher leakage currents than the B-VB detector ones, especially at high bias voltages. As experimentally verified in recent works [39,40], this difference is due to the different barrier heights of detectors: 1.1 e V for B-VB and 0.9 eV for THM grown detectors. The reason of this difference is unclear, probably, due to the different impact of electroless process on the crystal surfaces. As shown in Fig. 4, the B-VB grown CZT detectors, at high bias voltage operation (10000 V/cm), can be very competitive with the Al/CdTe/Pt detectors with rectifying contacts: the leakage current of the IMEM 3 detector is only 7 times greater than the CdTe detector one.

The charge transport properties of the detectors were also investigated through the estimation of the mobility-lifetime product of the electrons $\mu_e\tau_e$. To evaluate the $\mu_e\tau_e$, we irradiated the detectors from the cathode side, by using the 22.1 keV line of the ^{109}Cd source, and the energy spectra at different bias voltages were measured. The measured charge collection efficiencies of two samples at 22.1 keV vs. the bias voltage are reported in Fig. 5. The experimental points are fitted with the simplified Hecht equation [41]. The estimated $\mu_e\tau_e$ values (5-10 ·10^{-3} cm^2/V) for the THM grown detectors are in agreement with the typical values presented in the literature [12, 13, 25]; the B-VB grown CZT detectors are characterized by poorer charge transport properties as highlighted by the estimated $\mu_e\tau_e$ values (0.6-1.0 ·10^{-3} cm^2/V).

In the following sections, we will show as these properties and differences will be crucial in the spectroscopic performance of the CZT detectors, especially at high fluxes.

3.2 Low-rate response of the detectors

3.2.1 Room temperature measurements

The time-stability of the detectors was first investigated. ^{241}Am and ^{57}Co spectra were measured, by using an electric field of 2000 V/cm, and all detectors showed good time-stability within a time window of 30 minutes, in agreement with the literature [1-3]. All energy spectra were measured by using the slow PSHA with a ST = 9 µs (the same performance were obtained by using an analog gaussian shaping amplifier, with shaping time constants of 1-2 µs, and a multichannel analyzer). Fig. 6 shows an overview of the energy resolution (FWHM) at 59.5 keV (^{241}Am source) of the detectors at different bias voltages. Generally, similar low-rate performance (energy resolution around 4% at 59.5 keV) for all CZT detectors were measured, but obtained at different bias voltages. A comparison of the thin CZT detectors with the Al/CdTe/Pt detector (0.75 mm thick) is also shown in Fig. 6a: energy resolution of about 3% at 59.5 keV, measured with the same electronics [36]. This result highlights as thin CdTe detectors with rectifying contacts, that are characterized by low bias induced polarization even at room temperature [36], are still the best choice for the development of low-energy spectrometers (energy range<60 keV).

Concerning the CZT detectors, the B-VB grown CZT detectors allow higher bias voltage operation (> 8000 V/cm) than the THM detector ones (< 2000 V/cm), in perfect agreement with the measured electrical characteristics. The ^{241}Am and ^{57}Co spectra measured with the IMEM 3 detector (900 V) are shown in Figs. 7 and 8. Fig. 9a shows a zoom of the 122 keV photopeaks of the ^{57}Co spectra, measured with IMEM 3 and REDLEN 2.1 detectors at the same bias voltages (200 V). The shape (tailing) of the peaks clearly reflects the differences in the charge transport properties between B-VB and THM crystals. As shown in Fig. 9b, the effects of incomplete charge collection in B-VB grown CZT detectors are mitigated through the high bias voltage operation (900 V; IMEM 3).

3.2.2 Temperature effects

The time-stability of the detectors, in a time window of 30 minutes, was verified up to T = -15 °C. Fig. 10 shows the energy resolution (FWHM at 59.5 keV) vs. the bias voltage of the IMEM 3 detector at different temperatures. Generally, low spectral improvements characterize the detector up to T = -15 °C (similar results were obtained for all CZT detectors). The main result is that the temperature lowering allows to maintain good energy resolution even at high bias voltages. At low bias voltages (< 200 V), a degradation of the energy resolution by lowering the temperature was observed (Fig. 10). The temperature degradation of the energy resolution can be explained by the perturbation of the electric field of the detector, producing poor charge drift [18,19]. This is due to the formation of positive space charge in the bulk (accumulation of space charges at deep levels) that perturbs the electric field profile within the detector [18,19]. The temperature lowering delays the de-trapping process and increases the charge buildup. Due to the small investigated temperature range (258-298 K), this effect is more visible at low bias voltages. Table 2 reports the energy resolution of the IMEM 3 detector at room temperature and at T = 5 °C.

3.2.3 Pulse shape analysis

As previously discussed in the Materials and Methods section, the digital electronics is able to provide, beside the height (i.e. the energy) of the pulses, also the shape of the pulses: i.e. the peaking time of the slow SDL shaped pulses (the pulses selected by the PUR for the slow PSHA) and the time width of the fast SDL shaped pulses (all detected pulses by the fast PSHA). The correlation of the pulse shape with the pulse height is very helpful to mitigate the effects of incomplete charge collection, as widely reported in the literature [2,3,31]. Fig. 11a shows the peaking time distribution, measured with a fine time bin width of 1 ns, of the pulses from the slow PSHA (^{57}Co source, IMEM 3 detector). The distribution has an asymmetric shape with a tailing on the high peaking time side. As well known, the pulses with long peaking time values generally suffer from incomplete charge collection. By selecting the proper peaking time region (PTR), i.e. by performing a pulse shape discrimination (PSD), it is possible to improve the detector performance, but taking care of an excessive total count reduction. Fig. 11b shows the spectral improvements in the measured ^{57}Co spectrum by selecting the PTR of Fig.11a (red line); we selected a PTR able to produce no reduction of the counts in the photopeak centroid of the spectrum, with a percentage reduction of the total counts of 45 %.

Also the fast analysis is able to provide, beside the pulse height, the shape of all detected pulses, i.e. their time widths. As discussed in the description of the digital electronics, the time width of the SDL shaped pulses is related to the peaking time of the pulses and then a correlation with the incomplete charge collection effects can be performed. We stress that the fast PSHA generally gives energy spectra with poorer energy resolution than the slow PSHA one, but due to the lower dead time it allows higher throughputs, very important at high ICRs. In the following, we will show as the time width is also correlated to incomplete charge collection effects (Fig 12). Fig. 12 shows the time width distribution, measured with a time bin width of 10 ns, of the pulses from the fast PSHA (^{57}Co source, IMEM 3 detector) and the spectral improvements in the measured ^{57}Co spectrum after PSD. We selected a time width region (TWR, i.e. the red line of Fig. 12a) able to produce no reduction of the counts in the photopeak centroid of the spectrum, with a percentage reduction of the total counts of 33 %.

3.3 High-rate response of the detectors

3.3.1 Room temperature measurements

The time-stability of the detectors was verified, within a time window of 30 minutes, up to 1 Mcps (^{241}Am source). Fig. 13 shows the time stability of the spectroscopic response of the IMEM 3 detector (^{241}Am source) at ICR = 750 kcps (bias voltage of 1100 V and electric field of 11000 V/cm). The slow PSHA with a *ST* = 5 µs was used. Generally, the B-VB grown CZT detectors, due to their high bias voltage operation, are characterized by better high-rate performance than the THM grown CZT detector ones, as shown in Figs. 14 and 15.

As widely reported in the previous sections, the digital system is able to provide two different types of energy spectra: (a) energy spectra, from the slow PSHA, characterized by a fine energy resolution and a low throughput, and (b) energy spectra, from the fast PSHA, characterized by poor energy resolution and high throughput; moreover, both spectra are related to the distribution of the shape of the pulses, through the peaking time (slow PSHA) and the time with (fast PSHA). At high ICRs, we used the pulse shape to also mitigate the pile-up effects in the energy spectra (peak pile-up), as successfully employed in previous works [31-33]. Fig. 16 shows the ^{241}Am spectra measured at 750 kcps with the IMEM 3 detector (bias voltage of 1100 V), by using both the slow (Fig. 16a) and the fast (Fig. 16b) PSHA. Looking for the optimum energy resolution, the slow PSHA gives, after PSD, better performance (7 % FWHM at 59.5 keV) than the fast one (8.7 % FWHM at 59.5 keV). While, concerning the throughput, the fast PSHA is characterized, even after PSD, by higher throughput (61 % after PSD) than the slow one (2.1 % after PSD). Fig. 17 also shows the ^{57}Co spectra measured at ICR = 540 kcps. The mitigation of both incomplete charge collection and pile-up effects, due to the PSD, is clearly visible in the figures. Table 3 summarizes the high-rate spectroscopic performance of the IMEM 3 detector.

The high-rate response (ICR = 1 Mcps) of the 2.5 mm thick B-VB grown CZT detector (IMEM 2.2) to the ^{241}Am source is shown in Fig. 18. The detector, biased at 2000 V (electric field of 8000 V/cm), allows, at 1 Mcps, an energy resolution of 11.3 % FWHM at 59.5 keV. However, the response at higher energies (^{57}Co source) shows as a detector collapse starts to appear at 540 kcps (Fig. 19a). This is due to the high flux radiation induced polarization phenomena [7,18,19], producing a degradation of the electric field within the detectors. The electric field distortions are caused by the charge buildup created within the detector that strongly depends on the radiation characteristics (flux and energy) and the detector properties (thickness, bias voltage and charge transport properties) [18]. The charge buildup is generally more severe in crystals with poor charge transport properties (low $\mu_h \tau_h$ values) [18]. In fact, as shown in Fig. 19b, the THM CZT grown detector (REDLEN 2), despite its lower bias voltage operation (3000 V/cm) than the B-VB grown

CZT detector one (8000 V/cm), due to its better charge transport properties, didn’t show any detector collapses up to 1 Mcps.

3.3.2 Temperature effects

Fig. 20 shows the temperature effects on the ^{241}Am response of the 1 mm thick B-VB grown CZT detector (IMEM 3) at medium (Fig. 20a) and high (Fig. 20b) rates. At 240 kpcs, the spectra are characterized by similar energy resolution up to T = 5 °C, while at higher rates (750 kcps) the spectra start to degrade at T = 10 °C. These distortions are more severe at high energies (^{57} Co source, Fig. 21) and at higher thickness (Fig. 22a). At 1 Mcps, no distortions were observed for the 3 mm thick THM grown CZT detector (REDLEN 2) up to T = -15 °C (Fig. 22b). These results point out as the charge transport properties strongly influence the high-rate performance at low temperatures. The temperature lowering delays the de-trapping process and increases the charge buildup that is more severe for the B-VB grown CZT detectors, characterized by poorer charge transport properties that the THM grown CZT detector ones.

4. Conclusions

The performance of new boron oxide encapsulated vertical Bridgman (B-VB) grown CZT detectors were presented in this work. Thin (1 mm thick) and thick (2.5 mm) planar CZT detectors, with gold electroless contacts, were developed and comparisons with the travelling heater method (THM) grown CZT detectors, also developed by our group, were performed.

Concerning the physical properties, the B-VB grown CZT detectors are mainly characterized by:

(i) very low leakage currents at room temperature, even at high bias voltages: 38 nA/cm^2 at 10000 V/cm, allowing high bias voltage operation;

(ii) charge transport properties, characterized by a mobility-lifetime product of the electrons $\mu_e \tau_e$ of about 10^{-3} cm^2/V.

Despite the poorer charge transport properties of B-VB detectors than the THM ones ($\mu_e \tau_e$ of about 10^{-2} cm^2/V), these detectors allow higher bias voltage operation, due to their high barrier height: 1.1 e V for B-VB and 0.9 eV for THM grown CZT detectors [39,40].

Generally, the spectroscopic response of the B-VB detectors to monochromatic X-ray and gamma ray sources (^{241}Am, ^{57}Co) mainly highlights the following results:

(i) good room temperature performance: no bias induced polarization, mitigation of incomplete charge collection effects and good high-rate performance up to 1 Mcps (^{241}Am, 60 keV);

(ii) high flux radiation induced polarization phenomena at both room temperature, for the thick detector and high energy (^{57}Co source, 122.1 keV), and at low temperatures (T<10 °C) for all detectors.

At low rates, similar room temperature performance (energy resolution of about 4% at 59.5 keV) were measured for all CZT detectors (B-VB and THM grown CZT detectors), but obtained at different optimum bias voltages. The B-VB grown CZT detectors allow higher bias voltage operation (> 8000 V/cm) than the THM detector ones (< 2000 V/cm), in perfect agreement with the measured electrical characteristics. Incomplete charge collection effects were mitigated by using the digital pulse shape analysis. Spectral improvements in the measured ^{57}Co spectra were obtained after the pulse shape discrimination (PSD): the energy resolution improves from 3.6 % to 2.6 % at 122 keV after PSD, with no reduction of the counts in the photopeak centroid of the spectrum and a percentage reduction of the total counts of 45 %.

At high rates, the B-VB grown CZT detectors, due to their high bias voltage operation, are characterized by better performance than the THM grown CZT detector ones. At room temperature, the detectors (both thin and thick detectors) didn’t show any radiation induced polarization phenomena up to 1 Mcps (^{241}Am spectra). High-rate ^{241}Am spectra were measured with an energy resolution of 8.7 % FWHM at 59.5 keV and throughput of 61 % at 750 kcps. Polarization effects start to appear at high energies (^{57}Co spectra at 540 kcps) for the thick detector. High flux radiation induced polarization effects were also observed at low temperatures ($T \leq 10$ °C), with spectral degradations even for the thin detector at 60 keV (^{241}Am spectra at 750 kcps). Due to their better charge transport properties, these effects were not observed for the THM CZT grown detectors, despite their poor high rate performance.

Acknowledgment

This work was supported by the Italian Ministry for Education, University and Research (MIUR) under PRIN Project No. 2012WM9MEP.

The authors would like to acknowledge the technical staff of the laboratory at DiFC of Palermo, Mr. Marcello Mirabello and Dr. Michele Quartararo for their technical assistance.

References

[1] T. Takahashi, S. Watanabe, IEEE Transactions on Nuclear Science 48 (2001) 950.

[2] A. Owens, Journal of Synchrotron Radiation 13 (2006) 143.

[3] S. Del Sordo et al., Sensors 9 (2009) 3491.

[4] L. Abbene, S. Del Sordo, Comprehensive Biomedical Physics 8 (2014) 285.

[5] K. Taguchi et al., Med. Phys. 40 (2013) 100901.

[6] J. S. Iwanczyk et al., IEEE Transactions on Nuclear Science 56 (2009) 535.

[7] C. Szeles et al., IEEE Transactions on Nuclear Science 55 (2008) 572.

[8] E. Fredenberg et al., Nuclear Instruments and Methods in Physics Research Section A 613 (2010) 156.

[9] K. Ogawa et al., Nuclear Instruments and Methods in Physics Research Section A 664 (2012) 29.

[10] L. Abbene et al., Nuclear Instruments and Methods in Physics Research Section A 777 (2015) 54.

[11] M. D. Wilson et al., JINST 10 (2015) P10011.

[12] H. Chen et al., IEEE Transactions on Nuclear Science 54 (2007) 811.

[13] S. A. Awadalla et al, Nuclear Instruments and Methods in Physics Research Section A 764 (2014) 193.

[14] L. Abbene, G. Gerardi, A. A. Turturici, S. Del Sordo, F. Principato, Nuclear Instruments and Methods in Physics Research Section A 730 (2013) 135.

[15] I. Farella et al., IEEE Transactions on Nuclear Science 56 (2009) 1736.

[16] F. Principato et al., Nuclear Instruments and Methods in Physics Research Section A 730 (2013) 141.

[17] A. A. Turturici et al., Nuclear Instruments and Methods in Physics Research Section A 795 (2015) 58.

[18] D. S. Bale et al., Physical Review B 77 (2008) 035205.

[19] P. J. Sellin et al., Applied Physics Letters 96 (2010) 133509.

[20] M. Zha et al., Journal of Crystal Growth 237 (2002) 1720.

[21] A. Zappettini et al., IEEE Transactions on Nuclear Science 58 (2009) 1743.

[22] A. Zappettini et al., Journal of Crystal Growth 307 (2007) 283.

[23] N. Zambelli et al., JINST 7 (2012) P08022.

[24] N. Auricchio et al., Journal of Applied Physics 110 (2011) 124502.

[25] H. Chen et al., Journal of Applied Physics 103 (2008) 014903.

[26] G. Gerardi, L. Abbene, Nuclear Instruments and Methods in Physics Research Section A 768 (2014) 46.

[27] L. Abbene, G. Gerardi, Journal of Synchrotron Radiation 22 (2015) 1190.

[28] L. Abbene et al., Nuclear Instruments and Methods in Physics Research Section A 730 (2013) 124.

[29] L. Abbene, G. Gerardi, F. Principato, S. Del Sordo, R. Ienzi, G. Raso, Med. Phys. 37 (2010) 6147.

[30] L. Abbene, G. Gerardi, S. Del Sordo, G. Raso, Nuclear Instruments and Methods in Physics Research Section A 621 (2010) 447.

[31] L. Abbene, G. Gerardi, Nuclear Instruments and Methods in Physics Research Section A 654 (2011) 340.

[32] L. Abbene, G. Gerardi, F. Principato, S. Del Sordo, G. Raso, Sensors 12 (2012) 8390.

[33] L. Abbene et al., JINST 8 (2013) P07019.

[34] G.F. Knoll, Radiation Detection and Measurement, third ed., Wiley, New York, 2000.

[35] F. Principato et al., Journal of Applied Physics 112 (2012) 094506.

[36] L. Abbene et al., IEEE Nuclear Science Symposium Conference Record (2011), 4636.

[37] A.E. Bolotnikov et al., Nuclear Instruments and Methods in Physics Research Section A 481 (2002) 395.

[38] L. Marchini et al., IEEE Transaction on Nuclear Science 56 (2009) 1823.

[39] A. A. Turturici et al., IEEE Nuclear Science Symposium Conference Record (2015), in press.

[40] A. A. Turturici et al., Nuclear Instruments and Methods in Physics Research Section A (2016), accepted.

[41] P. J. Sellin et al., IEEE Transactions on Nuclear Science 52 (2005) 3074.

LIST OF FIGURE CAPTIONS

FIG. 1. (color online) (a) The 1 mm thick B-VB grown CZT detector (cathode side view). (b) Schematic cross section view of the detectors.

FIG. 2. (color online) The main operations and outputs of the digital pulse processing (DPP) system.

FIG. 3. (color online) The current-voltage characteristics of the 1 mm thick B-VB grown CZT detector (IMEM 3) at T=25 °C and T=15°C. Low leakage current of 38 nA/cm^2 (T = 25°C) was measured even at very high electric field of 10000 V/cm.

FIG. 4. (color online) Comparison of the current-voltage characteristics, in the bias reverse region, among the (B-VB, THM) Au/CZT/Au detectors and an Al/CdTe/Pt detector (Acrorad, Japan).

FIG. 5. (color online) The normalized 22.1 keV photopeak centroid (i.e. the charge collection efficiency) at various cathode bias voltages for the IMEM 2.2 and REDLEN 2 detectors. The experimental points are fitted with the simplified Hecht equation [41]. The spectra were measured through the slow PSHA with a *ST* = 9 µs.

FIG. 6. (color online) Energy resolution (FWHM) at 59.5 keV vs. the bias voltage at room temperature for the thin (a) and the thick (b) CZT detectors. (a) The performance of an Al/CdTe/Pt detector, characterized by the same geometrical electrode layout and similar thickness (0.75 mm thick), are also shown. The spectra were measured through the slow PSHA with a *ST* = 9 μs (the same results were obtained by using an analog gaussian shaping amplifier, with shaping time constants of 1-2 μs, and a multichannel analyzer).

FIG. 7. (color online) The measured ^{241}Am spectrum for the IMEM 3 detector. The spectrum was measured through the slow PSHA with a *ST* = 9 μs.

FIG. 8. (color online) The measured ^{57}Co spectrum for the IMEM 3 detector. The spectrum was measured through the slow PSHA with a *ST* = 9 μs.

FIG. 9. (color online) Zoom of the 122 keV photopeaks of the ^{57}Co spectra, measured with IMEM 3 and REDLEN 2.1 detectors, (a) at the same bias voltages (200 V) and (b) at the optimum bias voltages.

FIG. 10. (color online) Energy resolution (FWHM) at 59.5 keV vs. the bias voltage at different temperatures for the IMEM 3 detector.

FIG. 11. (color online) (a) Peaking time distribution (black line) of the pulses from the slow PSHA (^{57}Co source, IMEM 3 detector) with a fine time bin width of 1 ns; the selected (red line) peaking time region (PTR) for the pulse shape discrimination (PSD). (b) ^{57}Co spectra after PSD (red line) and with no PSD (black line); the energy resolution after PSD is of 2.6 % FWHM at 122 keV (3.6 % with no PSD); the PSD produces no reduction of the counts in the photopeak centroid of the spectrum and a percentage reduction of the total counts of 45 %.

FIG. 12. (color online) (a) Time width distribution (black line) of the pulses from the fast PSHA (^{57}Co source, IMEM 3 detector) with a time bin width of 10 ns; the selected (red line) time width region (TWR) for the pulse shape discrimination (PSD). (b) ^{57}Co spectra after PSD (red line) and with no PSD (black line); the energy resolution after PSD is of 5.5 % FWHM at 122 keV (6.0 % with no PSD); the PSD produces no reduction of the counts in the photopeak centroid of the spectrum and a percentage reduction of the total counts of 33 %.

FIG. 13. (color online) The measured ^{241}Am spectra (ICR = 750 kcps) of the IMEM 3 detector, just after biasing (black line) and after 30 minutes (red line). The slow PSHA with a $ST = 5$ µs was used (throughput of 3 %). The Np L X-ray lines, typically of ^{241}Am sources, are shielded by the source holder.

FIG. 14. (color online) Energy resolution (FWHM) at 59.5 keV vs. (^{241}Am source) the bias voltage at room temperature for the IMEM 3 and REDLEN 2.1 detectors, at high ICRs. The slow PSHA with a $ST = 5$ µs was used (throughput of 3 %).

FIG. 15. (color online) The measured ^{241}Am spectra (ICR = 1Mcps) of the IMEM 2.2 and REDLEN 2 detectors. The slow PSHA with a *ST* = 4 µs was used (throughput of 2.4 %). The counts were normalized to the total number of the analyzed events in the spectra.

FIG. 16. (color online) The measured ^{241}Am spectra (ICR = 750 kcps) of the IMEM 3 detector, by using (a) the slow PSHA and (b) the fast PSHA. The slow PSHA (*ST* = 5 µs) gives an energy resolution of 8 % FWHM at 59.5 keV, with no PSD (throughput of 3%), and 7.1 % after PSD (throughput of 2.1 %). The fast PSHA (dead time = 270 ns) is characterized by energy an energy resolution of 8.7 % (both with PSD off and PSD on) with a throughput of 61 % after PSD. The reduction of pile-up effects, due to the PSD, is clearly visible (> 90 %).

FIG. 17. (color online) The measured ^{57}Co spectra (ICR = 540 kcps) of the IMEM 3 detector, by using the fast PSHA (dead time=270 ns) and PSD. Energy resolution values of 7 % FWHM at 122.1 keV (throughput of 87 %) and 5.7 % after PSD (throughput of 51 %) were measured. The reduction of both incomplete charge collection and pile-up effects, due to the PSD, is clearly visible.

FIG. 18. (color online) The measured ^{241}Am spectrum (ICR = 1 Mcps) of the IMEM 2.2 detector (2.5 mm thick). The fast PSHA with PSD was used (throughput of 49 %).

FIG. 19. (color online) High-rate ^{57}Co spectra measured with (a) the IMEM 2.2 detector and (b) the REDLEN 2 detector. A fast PSHA was used. A detector collapse is clearly visible for the B-VB

grown CZT detector at 540 kcps, while the THM grown detector keeps the typical shape of the ^{57}Co spectrum up to 1 Mcps.

FIG. 20. (color online) Temperature effects on the ^{241}Am spectra measured with the IMEM 3 detector (1 mm thick) at (a) medium (240 kcps) and (b) high (750 kcps) rates.

FIG. 21. (color online) Temperature effects on the ^{57}Co spectra measured with the IMEM 3 detector (1 mm thick) at 540 kcps.

FIG. 22. (color online) Temperature effects on the ^{241}Am spectra measured with the thick CZT detectors at 1 Mcps: (a) the B-VB grown CZT detector (IMEM 2.2, 2.5 mm thick) and (b) the THM grown CZT detector (REDLEN 2, 3 mm thick).

Figure 1

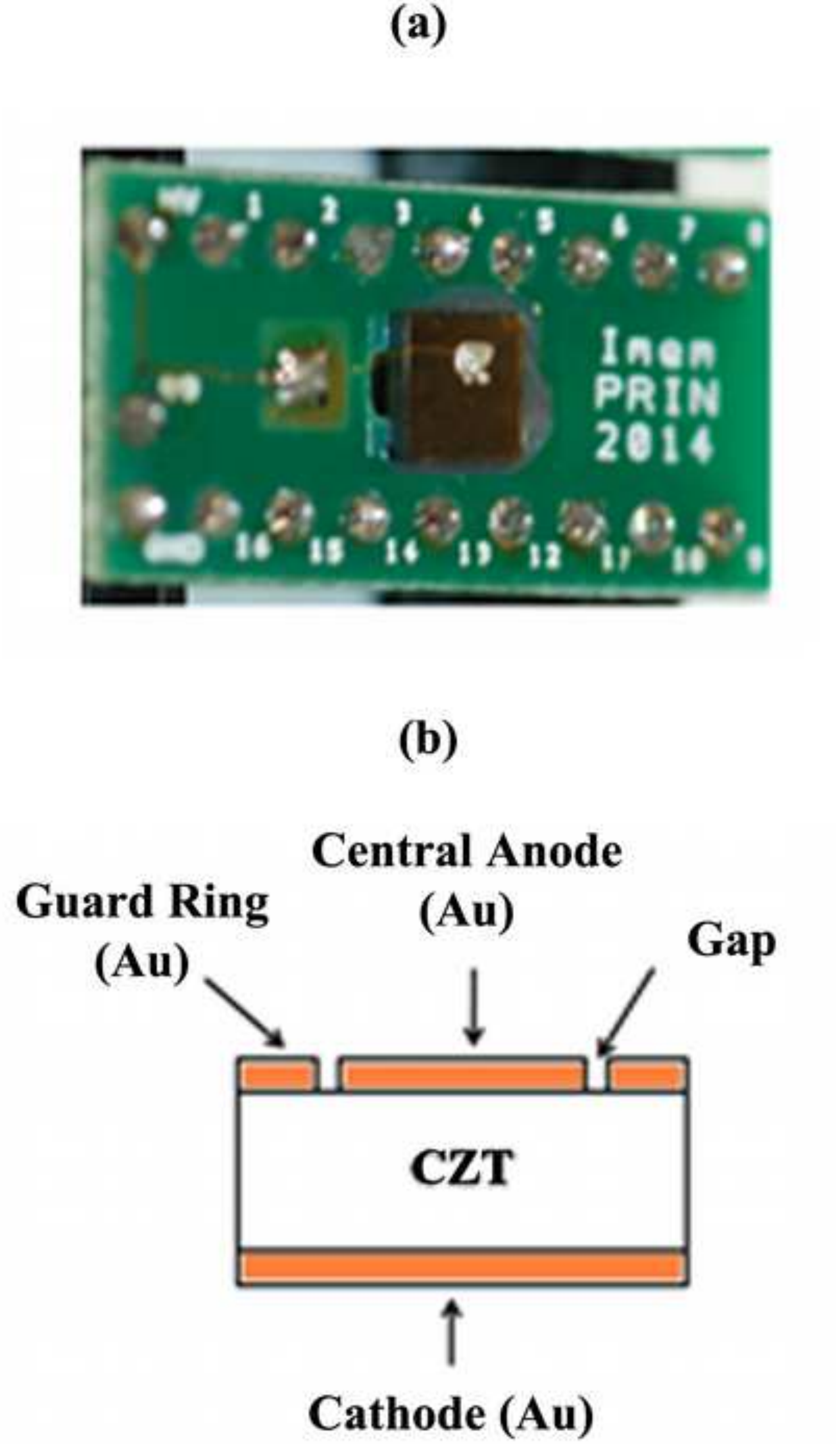
(a)
HV
1
2
3
4
5
6
7
8
GR
Imem
PRIN
2014
GND
16
15
14
13
12
11
10
9
(b)
Central Anode
(Au)
Guard Ring
(Au)
Gap
CZT
Cathode (Au)

Figure 2

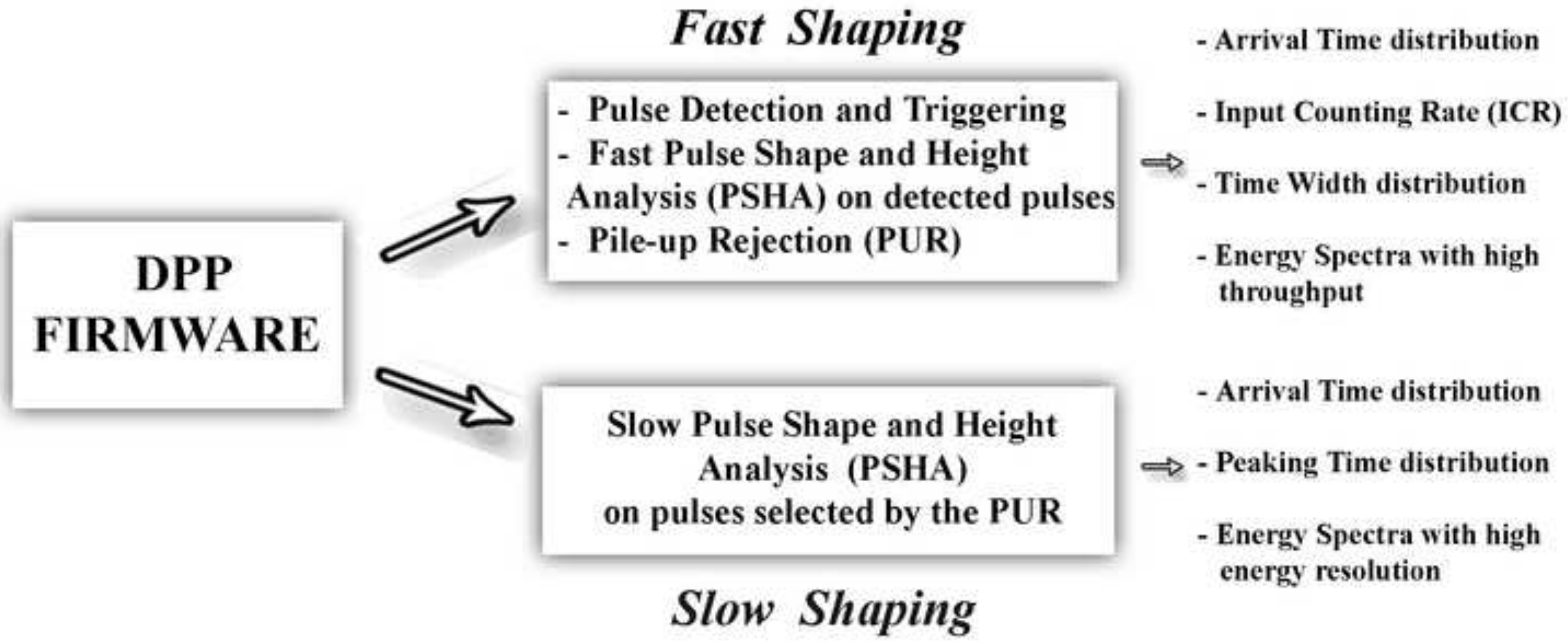
DPP FIRMWARE
Fast Shaping
- Pulse Detection and Triggering
- Fast Pulse Shape and Height Analysis (PSHA) on detected pulses
- Pile-up Rejection (PUR)
- Arrival Time distribution
- Input Counting Rate (ICR)
- Time Width distribution
- Energy Spectra with high throughput
Slow Pulse Shape and Height Analysis (PSHA) on pulses selected by the PUR
Slow Shaping
- Arrival Time distribution
- Peaking Time distribution
- Energy Spectra with high energy resolution

Figure 3

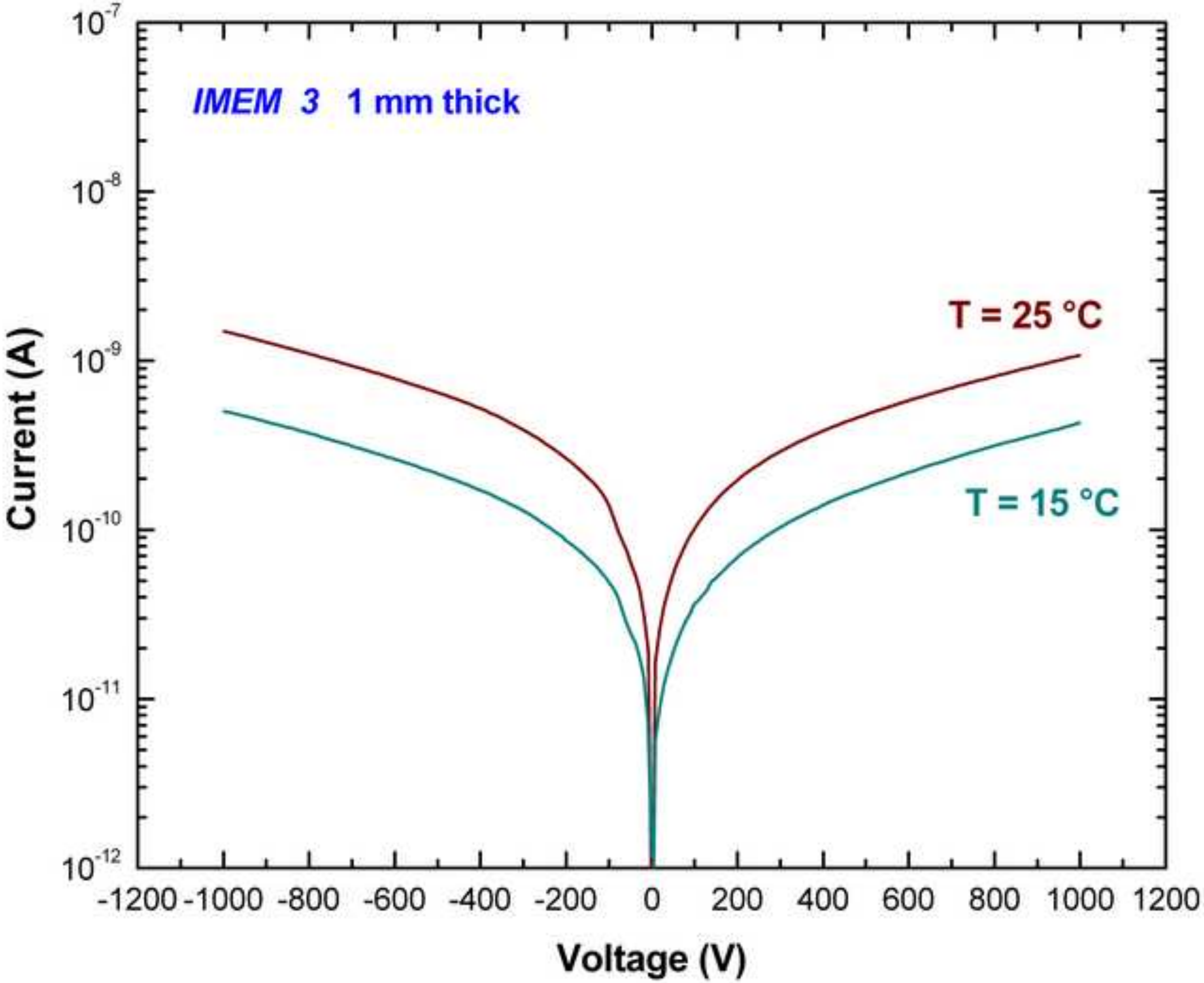
IMEM 3 1 mm thick
T = 25 °C
T = 15 °C
Current (A)
10^{-7}
10^{-8}
10^{-9}
10^{-10}
10^{-11}
10^{-12}
-1200
-1000
-800
-600
-400
-200
0
200
400
600
800
1000
1200
Voltage (V)

Figure 4

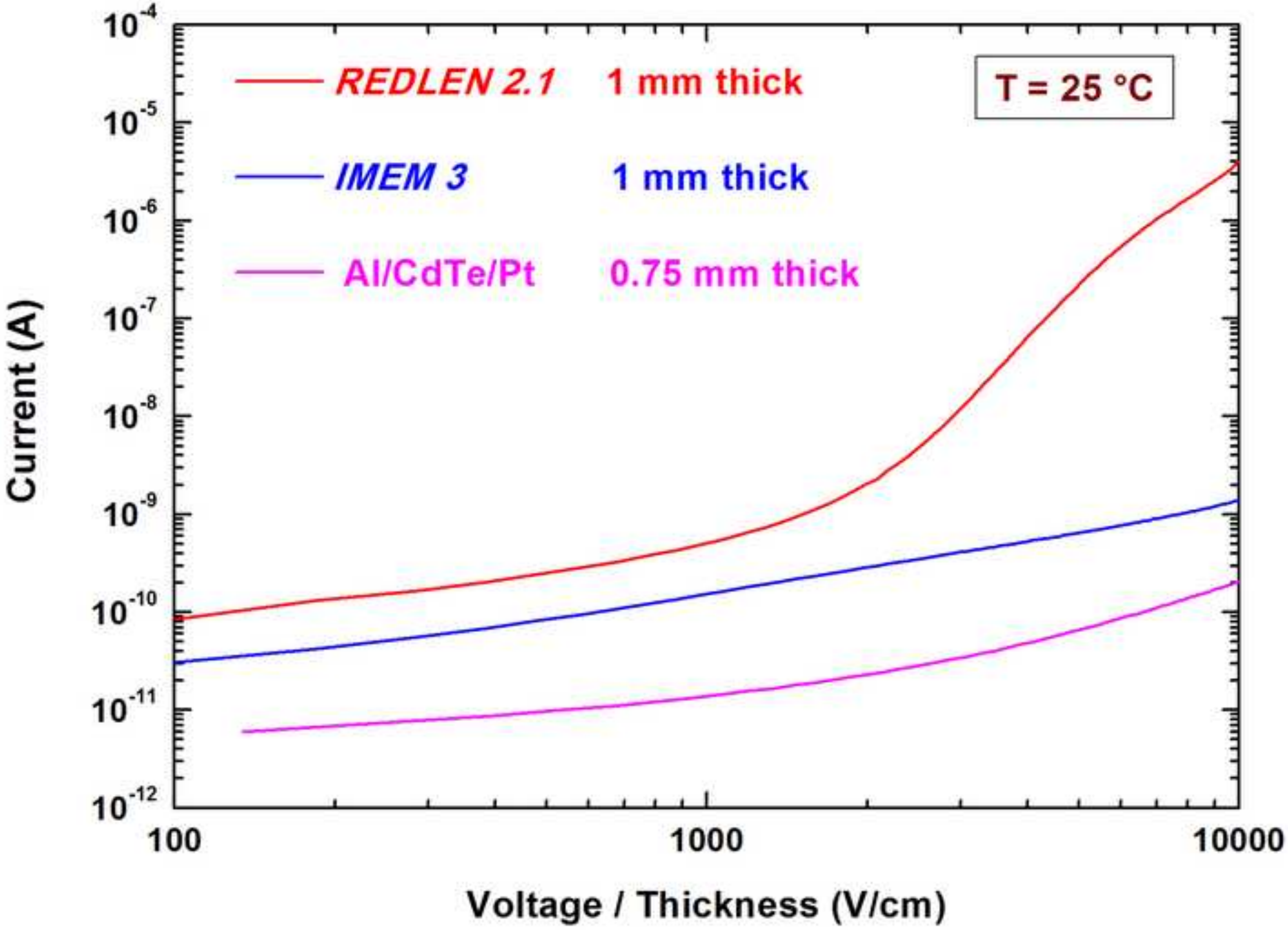
REDLEN 2.1 1 mm thick
IMEM 3 1 mm thick
Al/CdTe/Pt 0.75 mm thick
T = 25 °C
Current (A)
10^{-4}
10^{-5}
10^{-6}
10^{-7}
10^{-8}
10^{-9}
10^{-10}
10^{-11}
10^{-12}
100
1000
10000
Voltage / Thickness (V/cm)

Figure 5

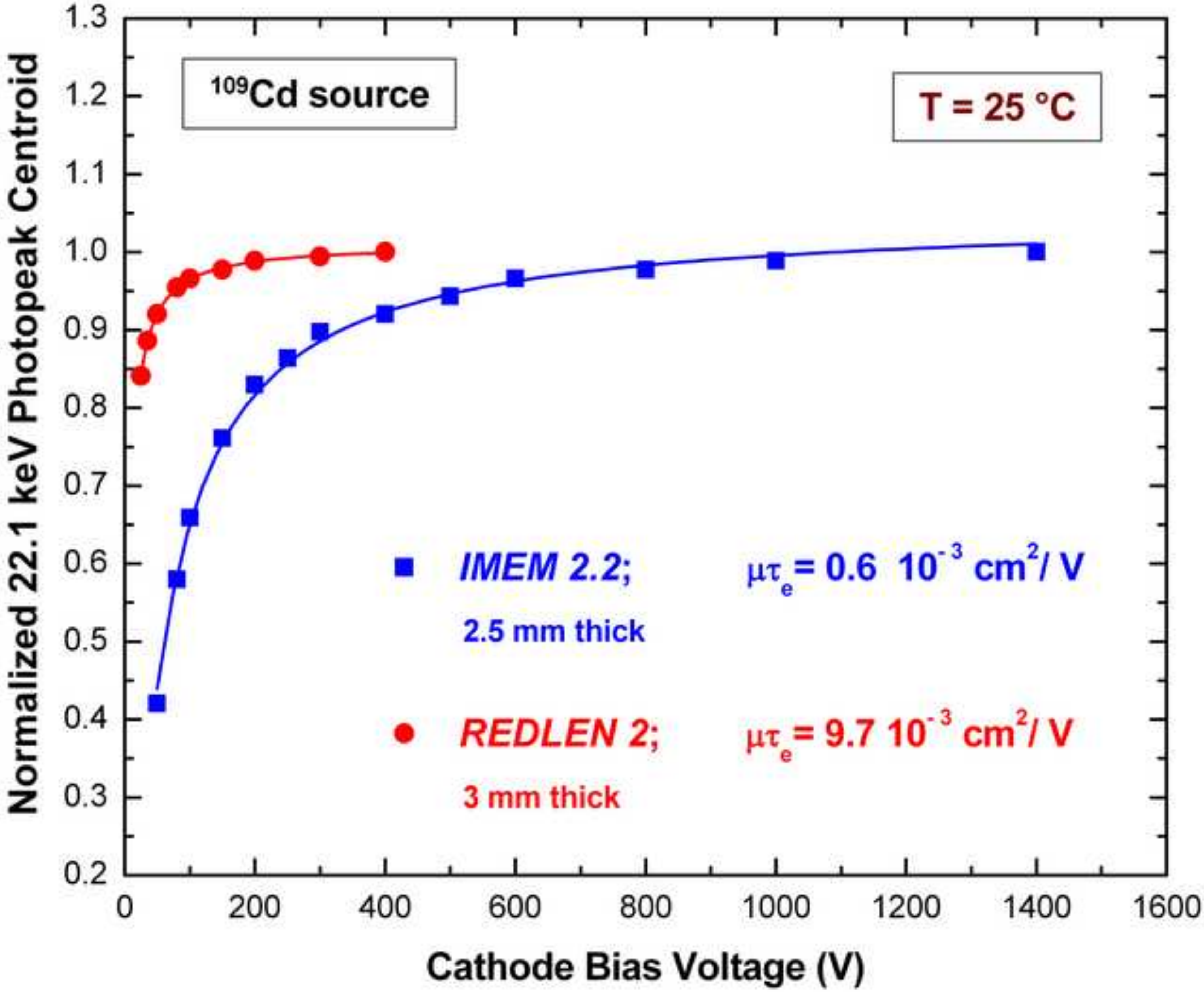

^{109}Cd source
T = 25 °C
Normalized 22.1 keV Photopeak Centroid
Cathode Bias Voltage (V)
1.3
1.2
1.1
1.0
0.9
0.8
0.7
0.6
0.5
0.4
0.3
0.2
0
200
400
600
800
1000
1200
1400
1600
■ IMEM 2.2; $\mu\tau_e$ = 0.6 10^{-3} cm^2/ V
2.5 mm thick
● REDLEN 2; $\mu\tau_e$ = 9.7 10^{-3} cm^2/ V
3 mm thick

Figure 6

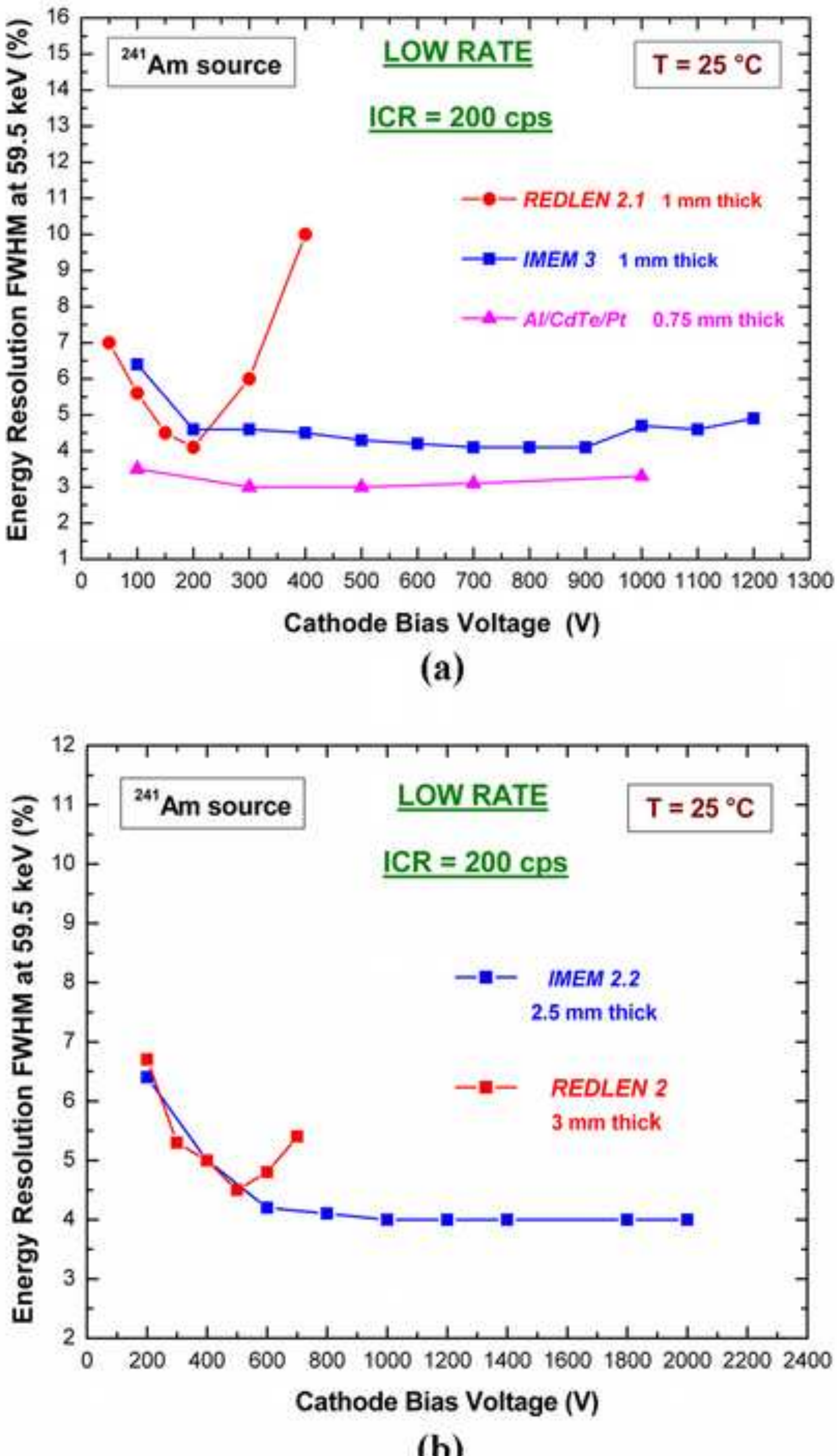

^{241}Am source
LOW RATE
ICR = 200 cps
T = 25 °C
REDLEN 2.1 1 mm thick
IMEM 3 1 mm thick
Al/CdTe/Pt 0.75 mm thick
Energy Resolution FWHM at 59.5 keV (%)
1
2
3
4
5
6
7
8
9
10
11
12
13
14
15
16
Cathode Bias Voltage (V)
0
100
200
300
400
500
600
700
800
900
1000
1100
1200
1300
^{241}Am source
LOW RATE
ICR = 200 cps
T = 25 °C
IMEM 2.2
2.5 mm thick
REDLEN 2
3 mm thick
Energy Resolution FWHM at 59.5 keV (%)
2
3
4
5
6
7
8
9
10
11
12
Cathode Bias Voltage (V)
0
200
400
600
800
1000
1200
1400
1600
1800
2000
2200
2400

(a)

(b)

Figure 7

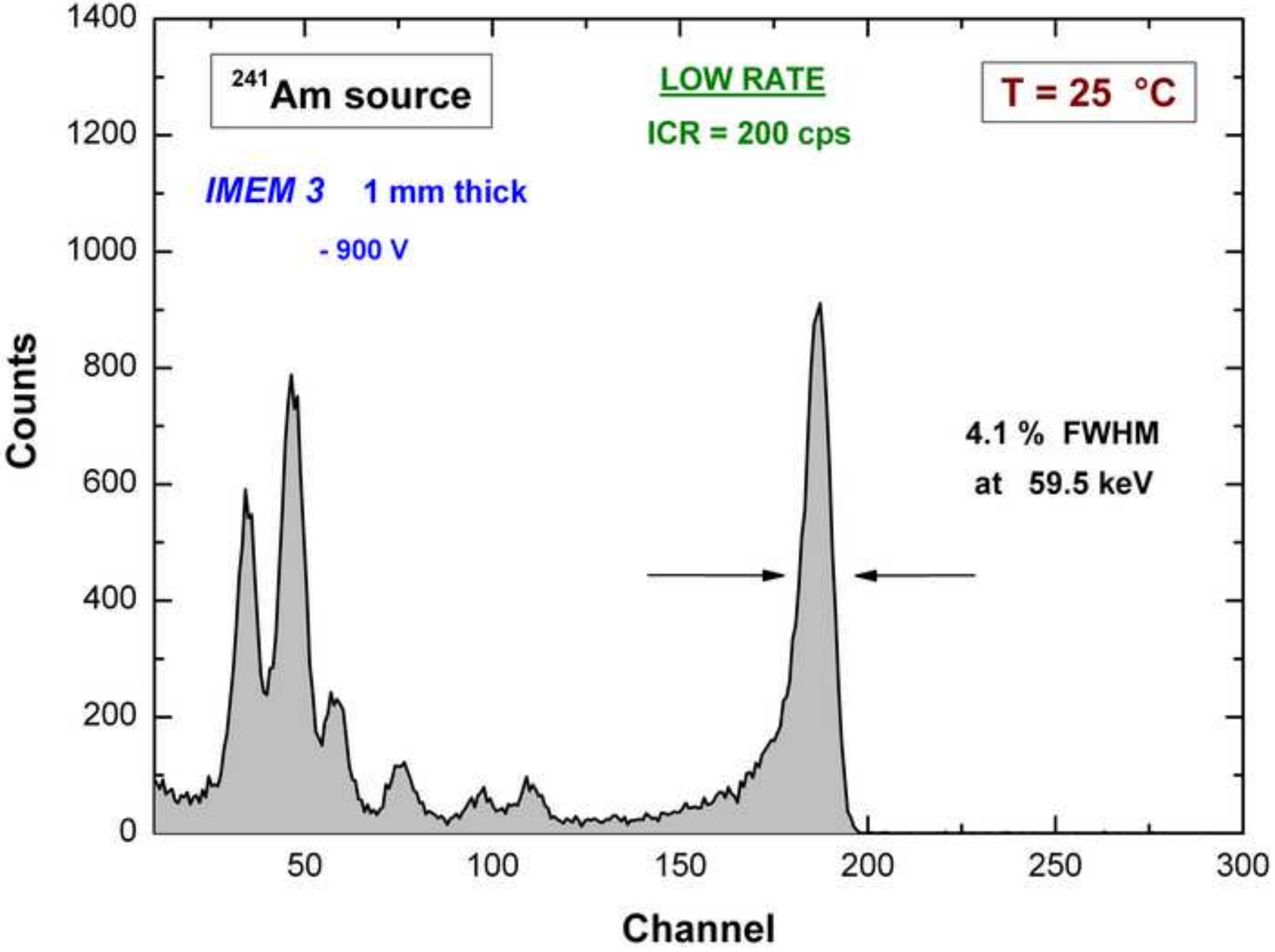

^{241}Am source
LOW RATE
ICR = 200 cps
T = 25 °C
IMEM 3 1 mm thick
- 900 V
4.1 % FWHM
at 59.5 keV
Counts
Channel
0
200
400
600
800
1000
1200
1400
50
100
150
200
250
300

Figure 8

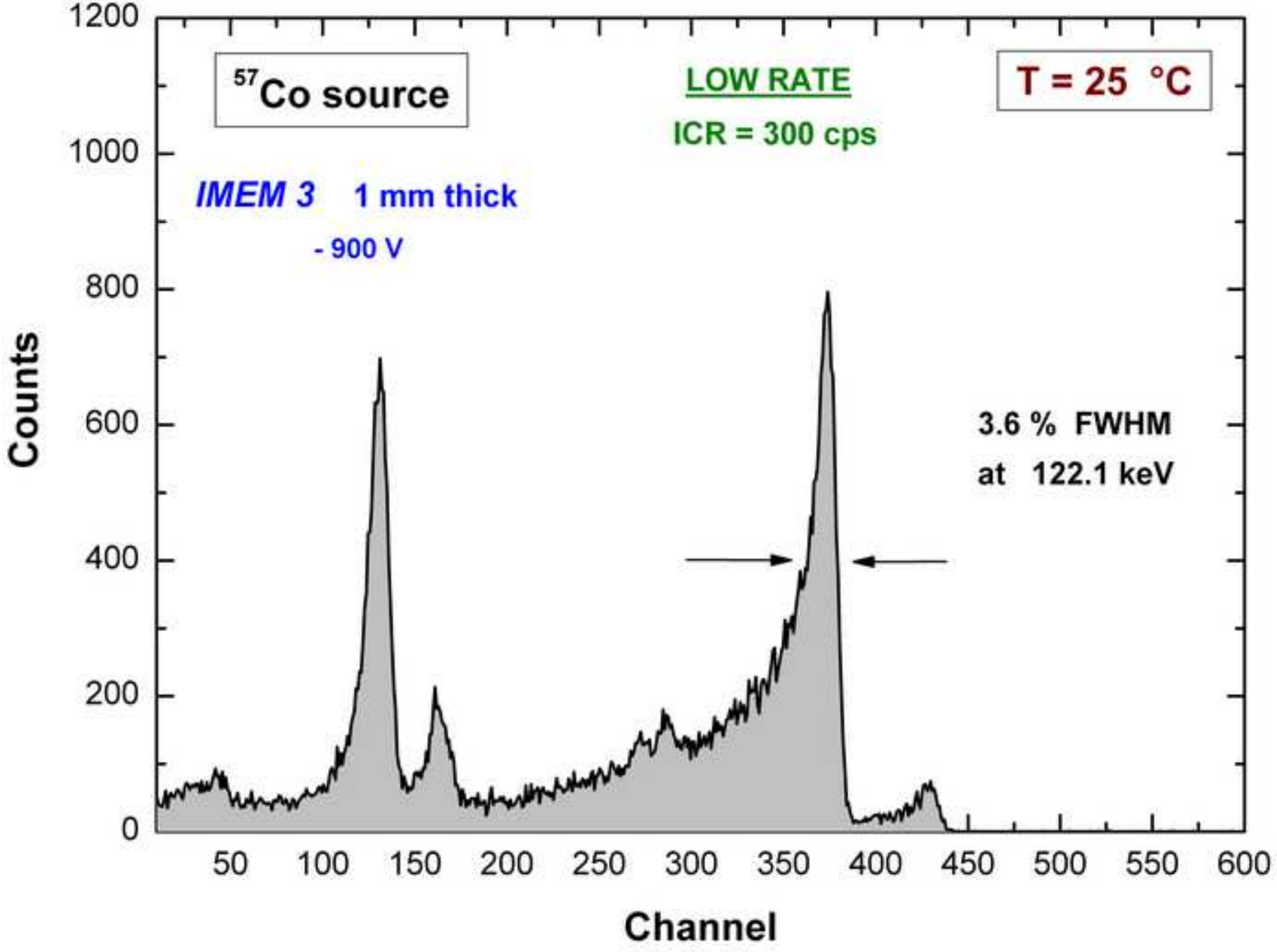

^{57}Co source
LOW RATE
ICR = 300 cps
T = 25 °C
IMEM 3 1 mm thick
- 900 V
3.6 % FWHM
at 122.1 keV
Counts
Channel
0
200
400
600
800
1000
1200
50
100
150
200
250
300
350
400
450
500
550
600

Figure 9

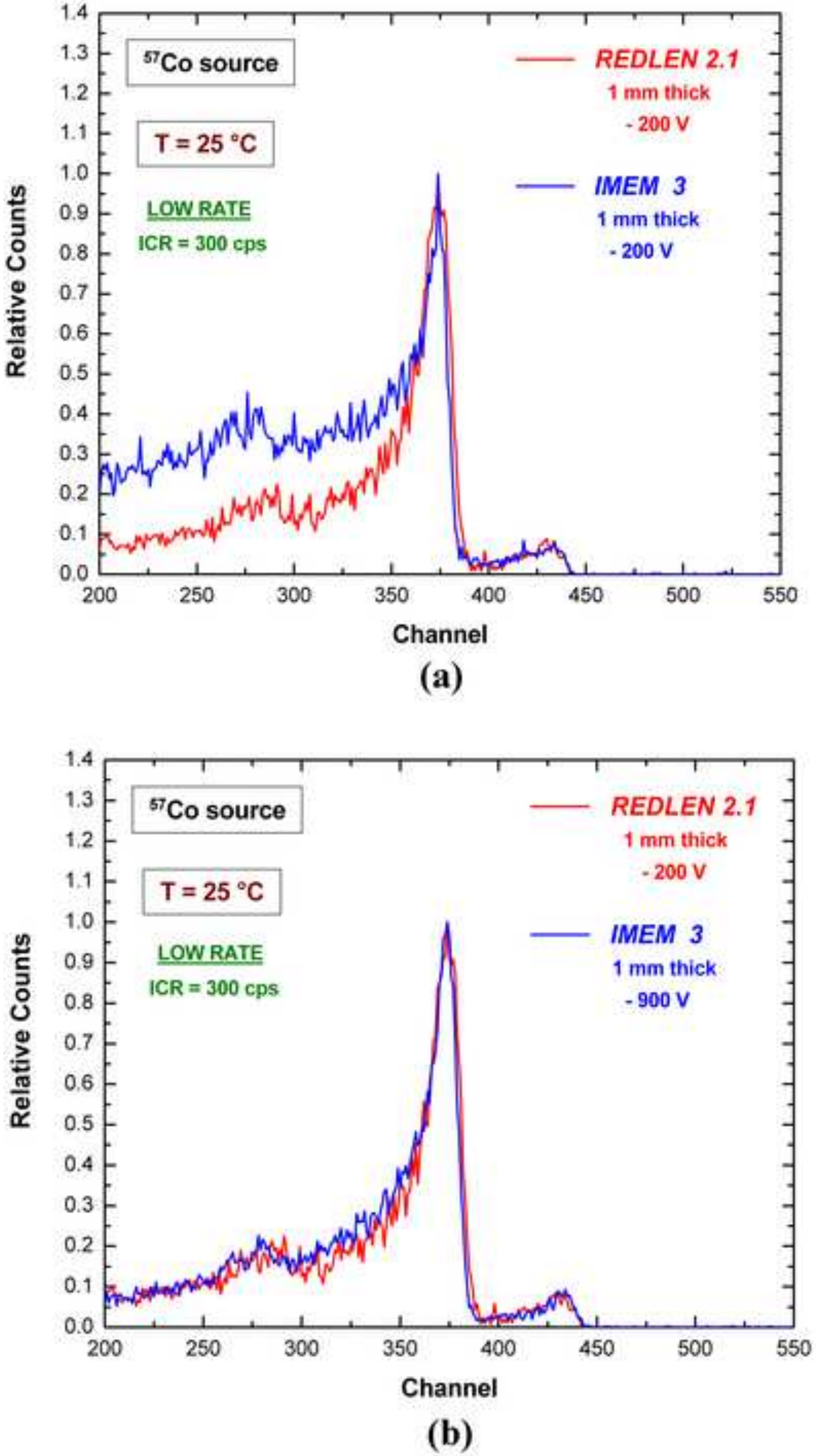

1.4
1.3
1.2
1.1
1.0
0.9
0.8
0.7
0.6
0.5
0.4
0.3
0.2
0.1
0.0
Relative Counts
^{57}Co source
T = 25 °C
LOW RATE
ICR = 300 cps
REDLEN 2.1
1 mm thick
- 200 V
IMEM 3
1 mm thick
- 200 V
200
250
300
350
400
450
500
550
Channel
(a)
1.4
1.3
1.2
1.1
1.0
0.9
0.8
0.7
0.6
0.5
0.4
0.3
0.2
0.1
0.0
Relative Counts
^{57}Co source
T = 25 °C
LOW RATE
ICR = 300 cps
REDLEN 2.1
1 mm thick
- 200 V
IMEM 3
1 mm thick
- 900 V
200
250
300
350
400
450
500
550
Channel
(b)

Figure 10

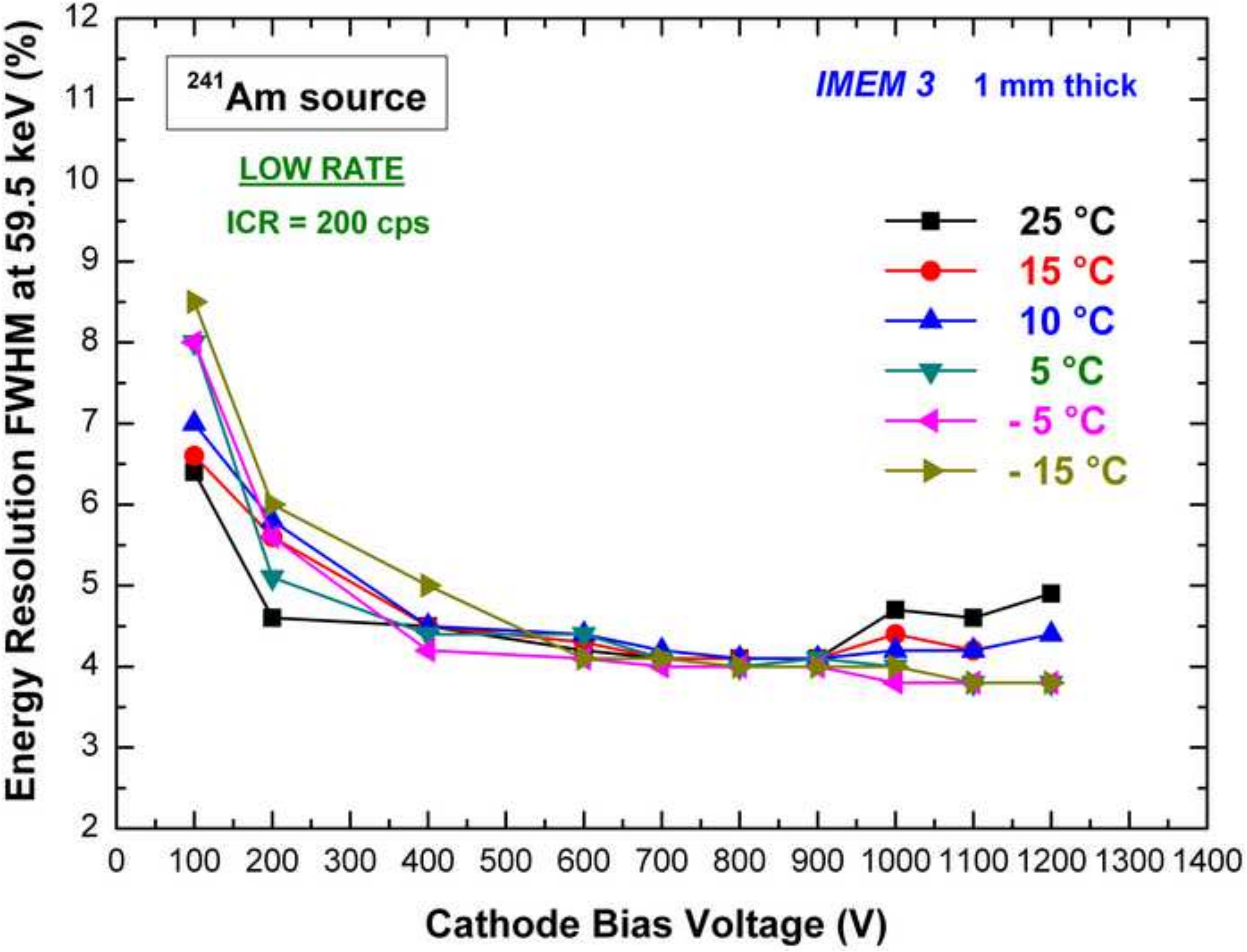

Energy Resolution FWHM at 59.5 keV (%)
12
11
10
9
8
7
6
5
4
3
2
^{241}Am source
LOW RATE
ICR = 200 cps
IMEM 3 1 mm thick
25 °C
15 °C
10 °C
5 °C
- 5 °C
- 15 °C
0
100
200
300
400
500
600
700
800
900
1000
1100
1200
1300
1400
Cathode Bias Voltage (V)

Figure 11

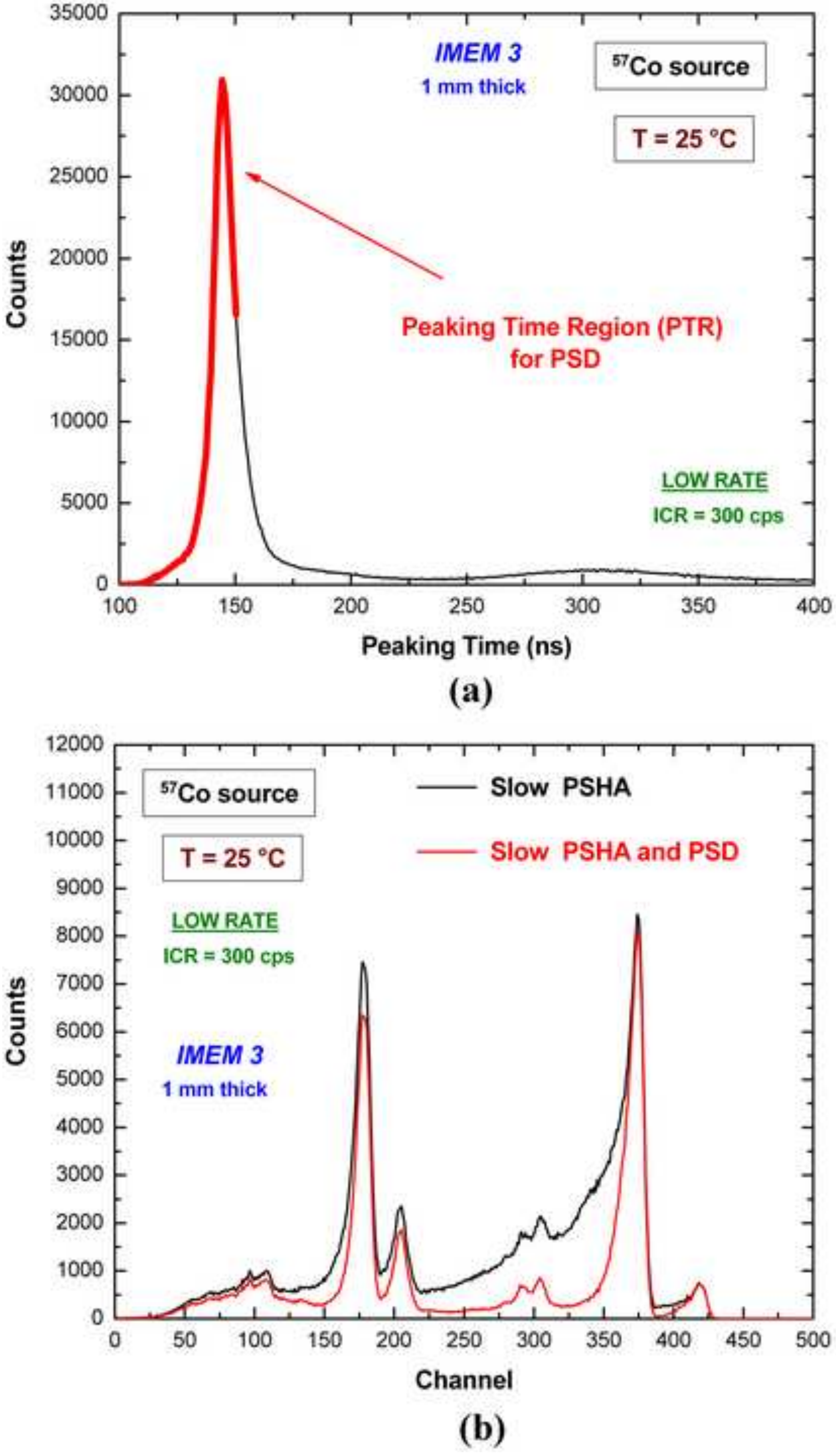
IMEM 3
1 mm thick
^{57}Co source
T = 25 °C
Peaking Time Region (PTR) for PSD
LOW RATE
ICR = 300 cps
Counts
0
5000
10000
15000
20000
25000
30000
35000
100
150
200
250
300
350
400
Peaking Time (ns)
(a)
^{57}Co source
T = 25 °C
Slow PSHA
Slow PSHA and PSD
LOW RATE
ICR = 300 cps
IMEM 3
1 mm thick
Counts
0
1000
2000
3000
4000
5000
6000
7000
8000
9000
10000
11000
12000
0
50
100
150
200
250
300
350
400
450
500
Channel
(b)

Figure 12

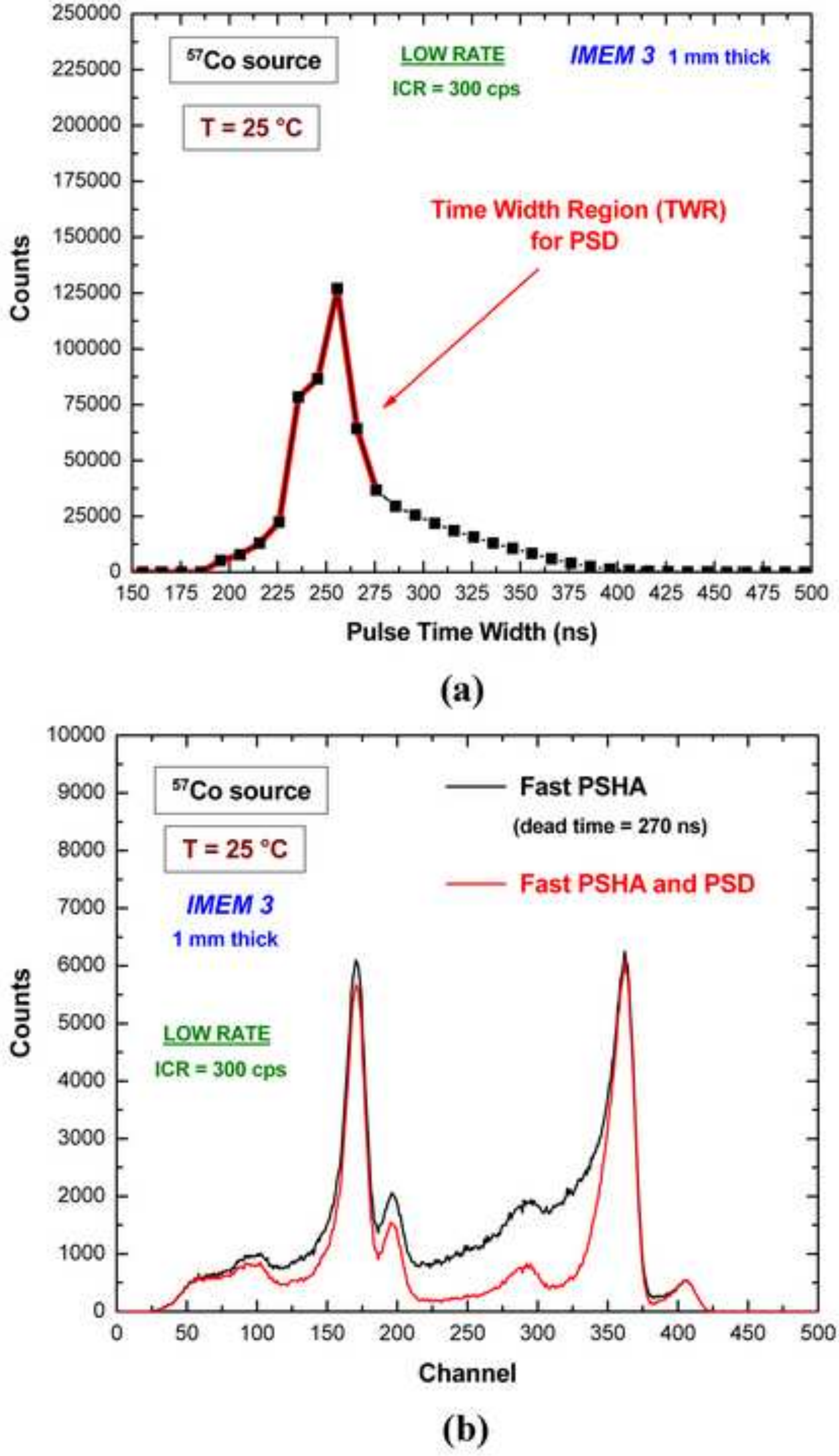
⁵⁷Co source
T = 25 °C
LOW RATE
ICR = 300 cps
IMEM 3 1 mm thick
Time Width Region (TWR) for PSD
Counts
0
25000
50000
75000
100000
125000
150000
175000
200000
225000
250000
150
175
200
225
250
275
300
325
350
375
400
425
450
475
500
Pulse Time Width (ns)
(a)
⁵⁷Co source
T = 25 °C
IMEM 3
1 mm thick
LOW RATE
ICR = 300 cps
Fast PSHA
(dead time = 270 ns)
Fast PSHA and PSD
Counts
0
1000
2000
3000
4000
5000
6000
7000
8000
9000
10000
0
50
100
150
200
250
300
350
400
450
500
Channel
(b)

Figure 13

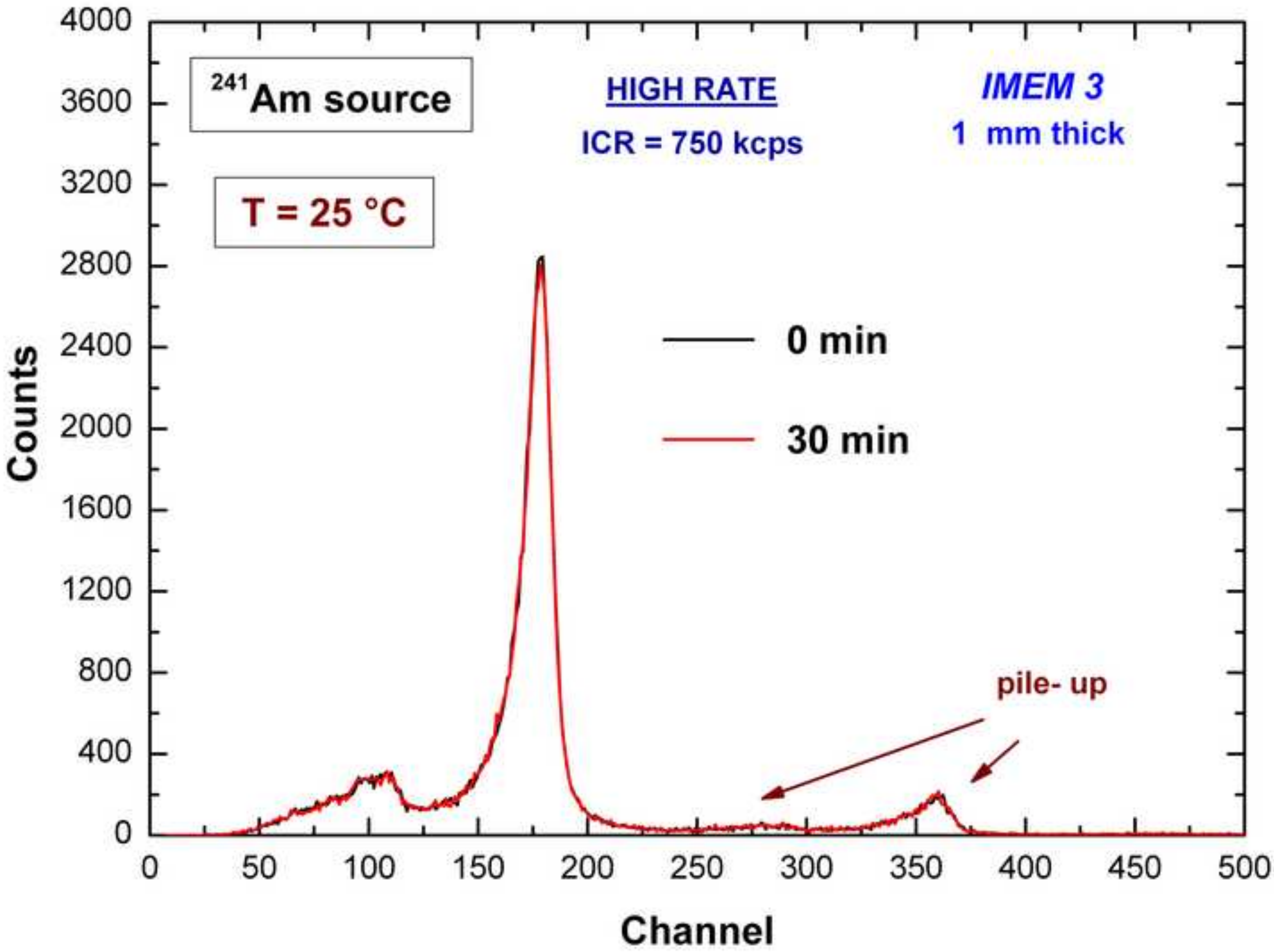

^{241}Am source
T = 25 °C
HIGH RATE
ICR = 750 kcps
IMEM 3
1 mm thick
0 min
30 min
pile- up
Counts
Channel
0
400
800
1200
1600
2000
2400
2800
3200
3600
4000
0
50
100
150
200
250
300
350
400
450
500

Figure 14

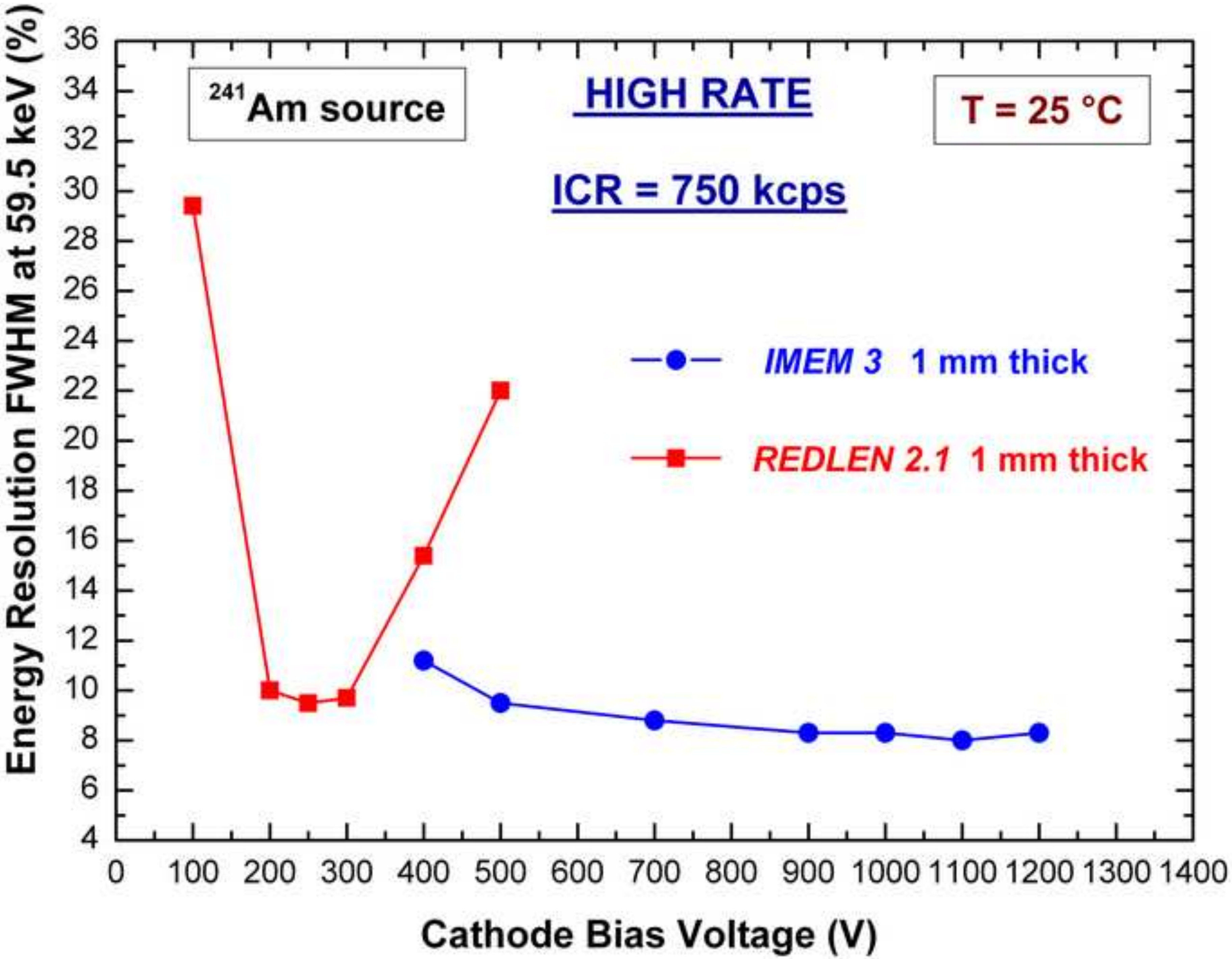

^{241}Am source
HIGH RATE
T = 25 °C
ICR = 750 kcps
IMEM 3 1 mm thick
REDLEN 2.1 1 mm thick
Energy Resolution FWHM at 59.5 keV (%)
36
34
32
30
28
26
24
22
20
18
16
14
12
10
8
6
4
0
100
200
300
400
500
600
700
800
900
1000
1100
1200
1300
1400
Cathode Bias Voltage (V)

Figure 15

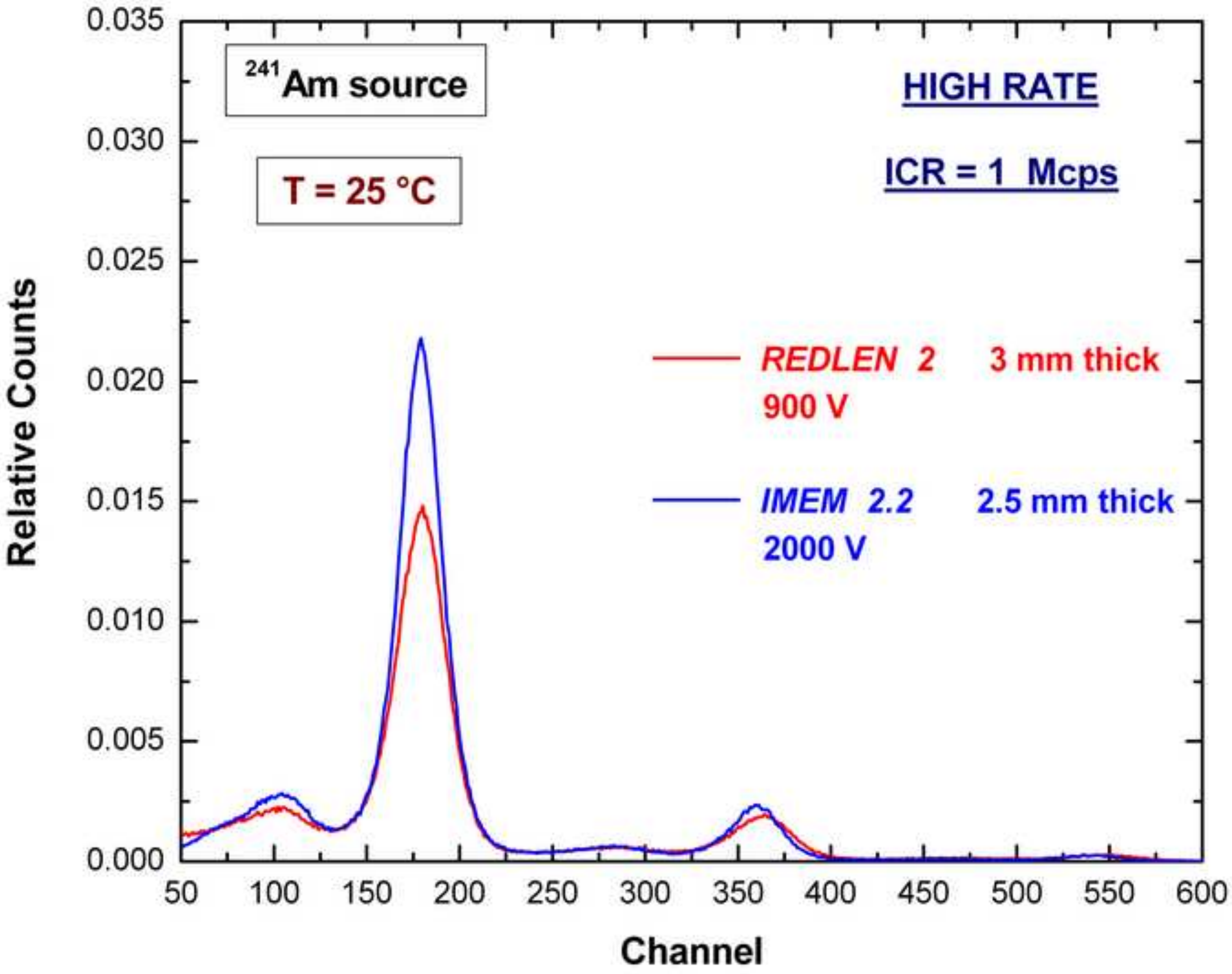

^{241}Am source
T = 25 °C
HIGH RATE
ICR = 1 Mcps
REDLEN 2 3 mm thick
900 V
IMEM 2.2 2.5 mm thick
2000 V
Relative Counts
0.035
0.030
0.025
0.020
0.015
0.010
0.005
0.000
50
100
150
200
250
300
350
400
450
500
550
600
Channel

Figure 16

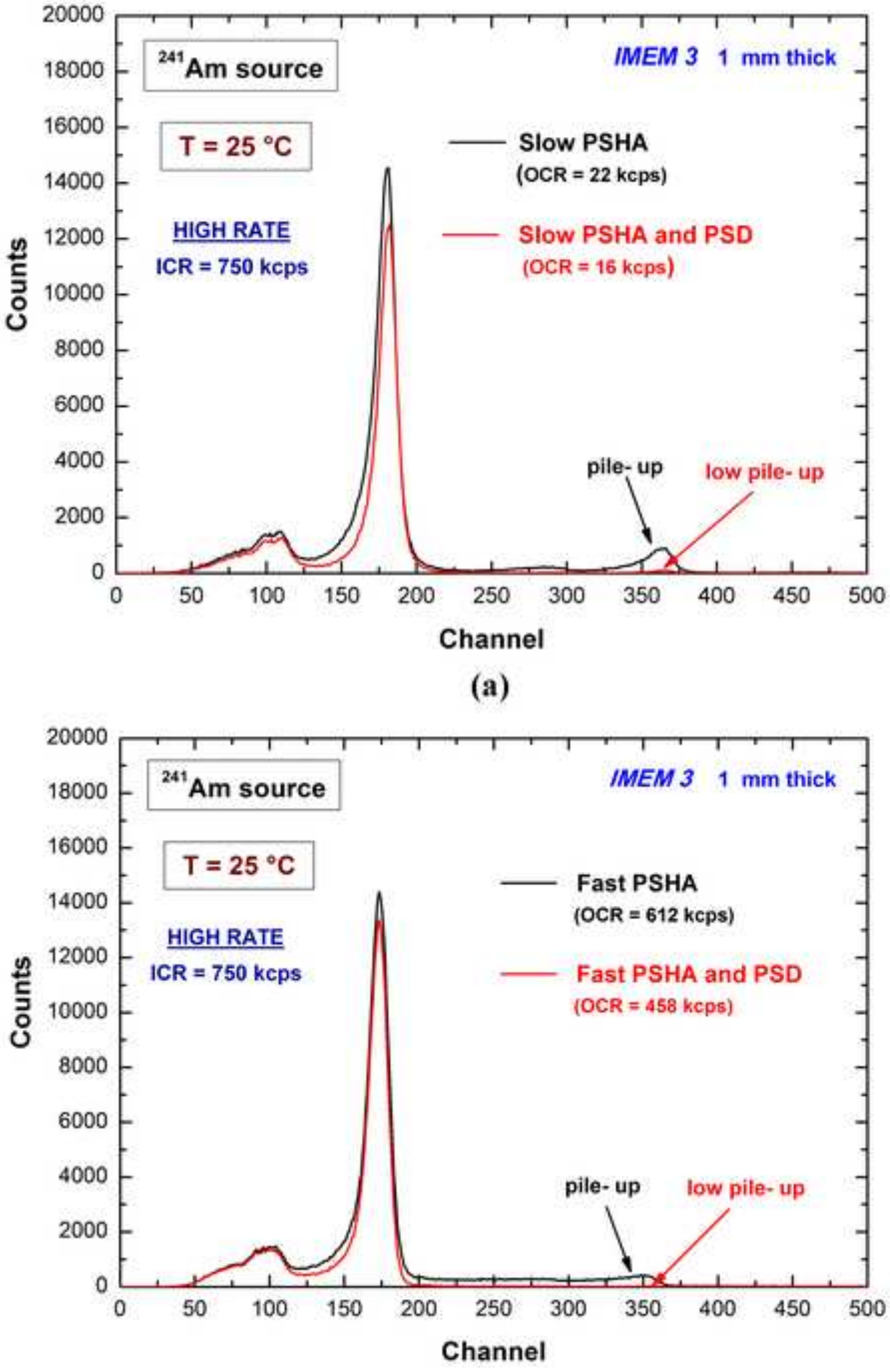
20000
18000
16000
14000
12000
10000
8000
6000
4000
2000
0
Counts
0
50
100
150
200
250
300
350
400
450
500
Channel
^{241}Am source
T = 25 °C
HIGH RATE
ICR = 750 kcps
IMEM 3 1 mm thick
Slow PSHA
(OCR = 22 kcps)
Slow PSHA and PSD
(OCR = 16 kcps)
pile- up
low pile- up
20000
18000
16000
14000
12000
10000
8000
6000
4000
2000
0
Counts
0
50
100
150
200
250
300
350
400
450
500
Channel
^{241}Am source
T = 25 °C
HIGH RATE
ICR = 750 kcps
IMEM 3 1 mm thick
Fast PSHA
(OCR = 612 kcps)
Fast PSHA and PSD
(OCR = 458 kcps)
pile- up
low pile- up

(a)

(b)

Figure 17

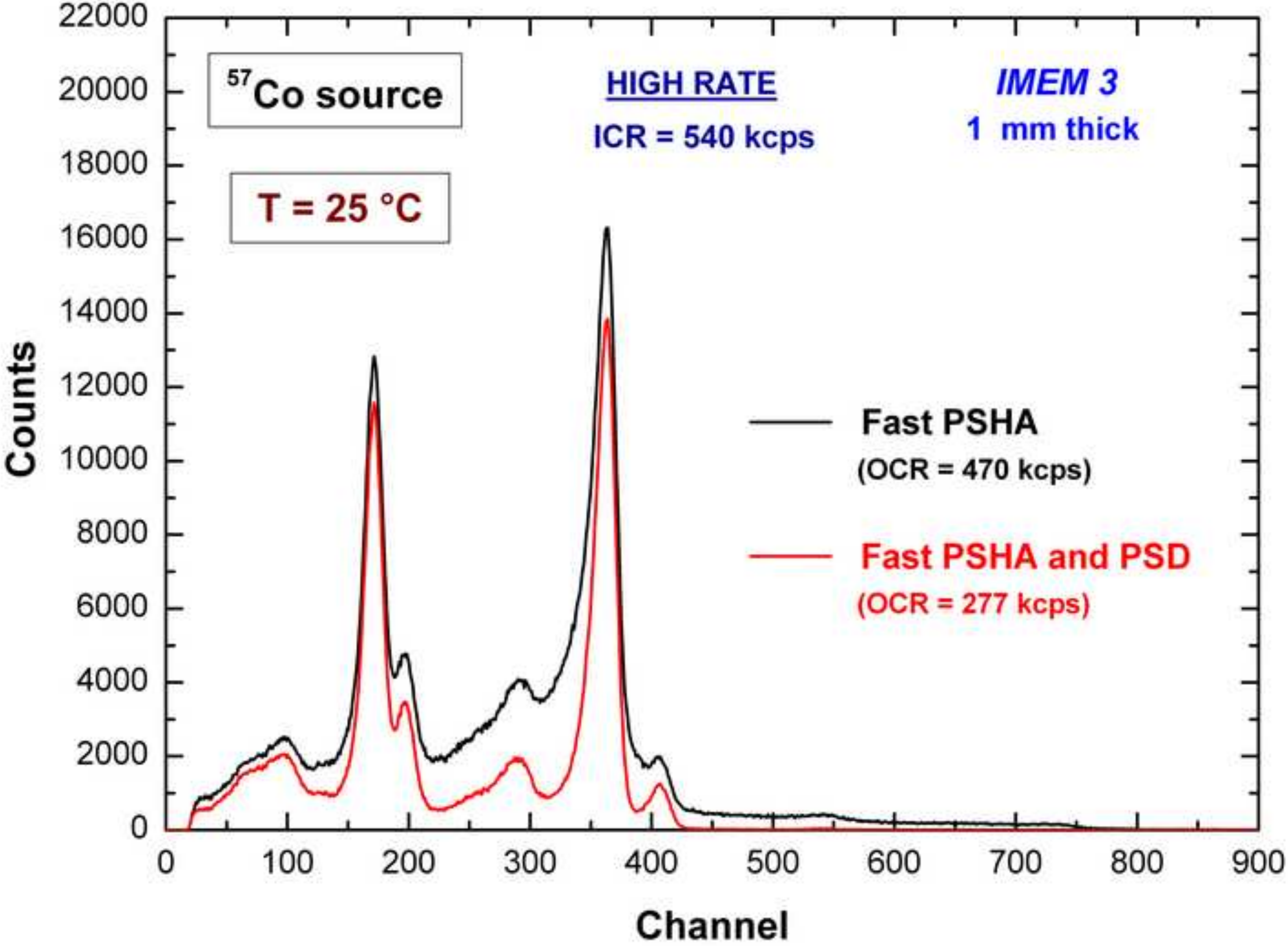

^{57}Co source
T = 25 °C
HIGH RATE
ICR = 540 kcps
IMEM 3
1 mm thick
Fast PSHA
(OCR = 470 kcps)
Fast PSHA and PSD
(OCR = 277 kcps)
Counts
Channel
0
2000
4000
6000
8000
10000
12000
14000
16000
18000
20000
22000
0
100
200
300
400
500
600
700
800
900

Figure 18

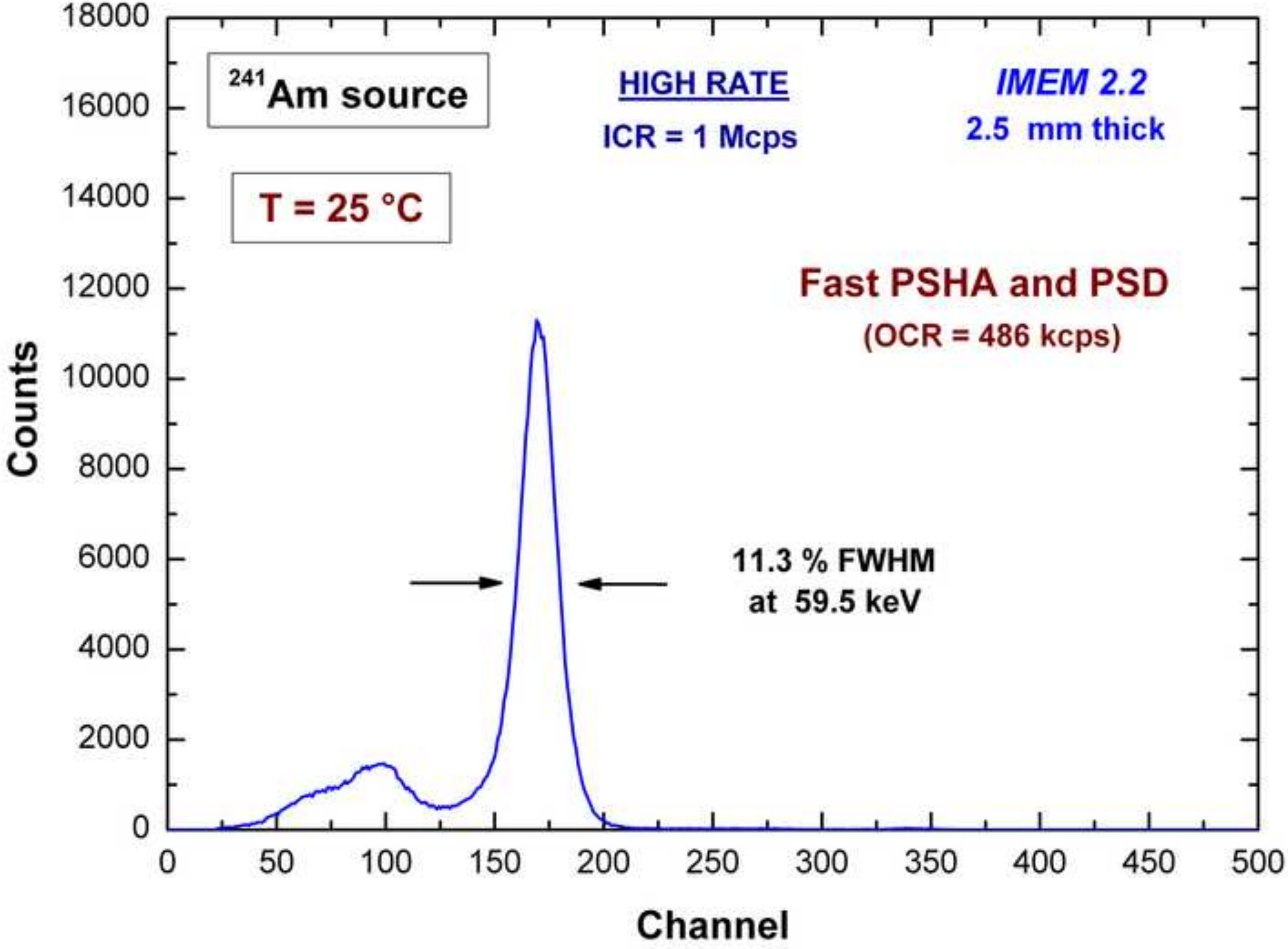

241Am source
T = 25 °C
HIGH RATE
ICR = 1 Mcps
IMEM 2.2
2.5 mm thick
Fast PSHA and PSD
(OCR = 486 kcps)
11.3 % FWHM
at 59.5 keV
Counts
Channel
0
2000
4000
6000
8000
10000
12000
14000
16000
18000
0
50
100
150
200
250
300
350
400
450
500

Figure 19

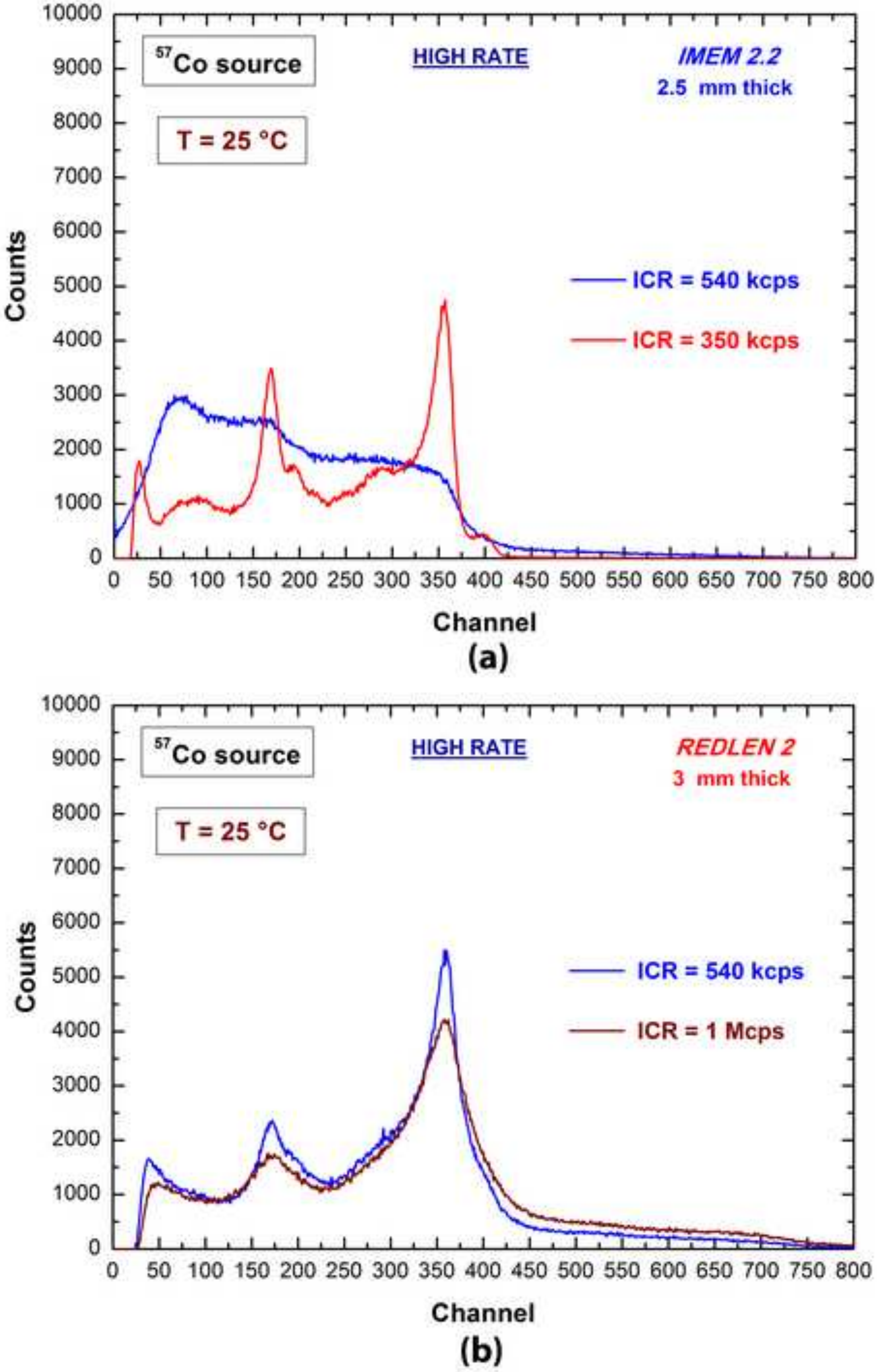

10000
9000
8000
7000
6000
5000
4000
3000
2000
1000
0
Counts
^{57}Co source
T = 25 °C
HIGH RATE
IMEM 2.2
2.5 mm thick
ICR = 540 kcps
ICR = 350 kcps
0 50 100 150 200 250 300 350 400 450 500 550 600 650 700 750 800
Channel
(a)
10000
9000
8000
7000
6000
5000
4000
3000
2000
1000
0
Counts
^{57}Co source
T = 25 °C
HIGH RATE
REDLEN 2
3 mm thick
ICR = 540 kcps
ICR = 1 Mcps
0 50 100 150 200 250 300 350 400 450 500 550 600 650 700 750 800
Channel
(b)

Figure 20

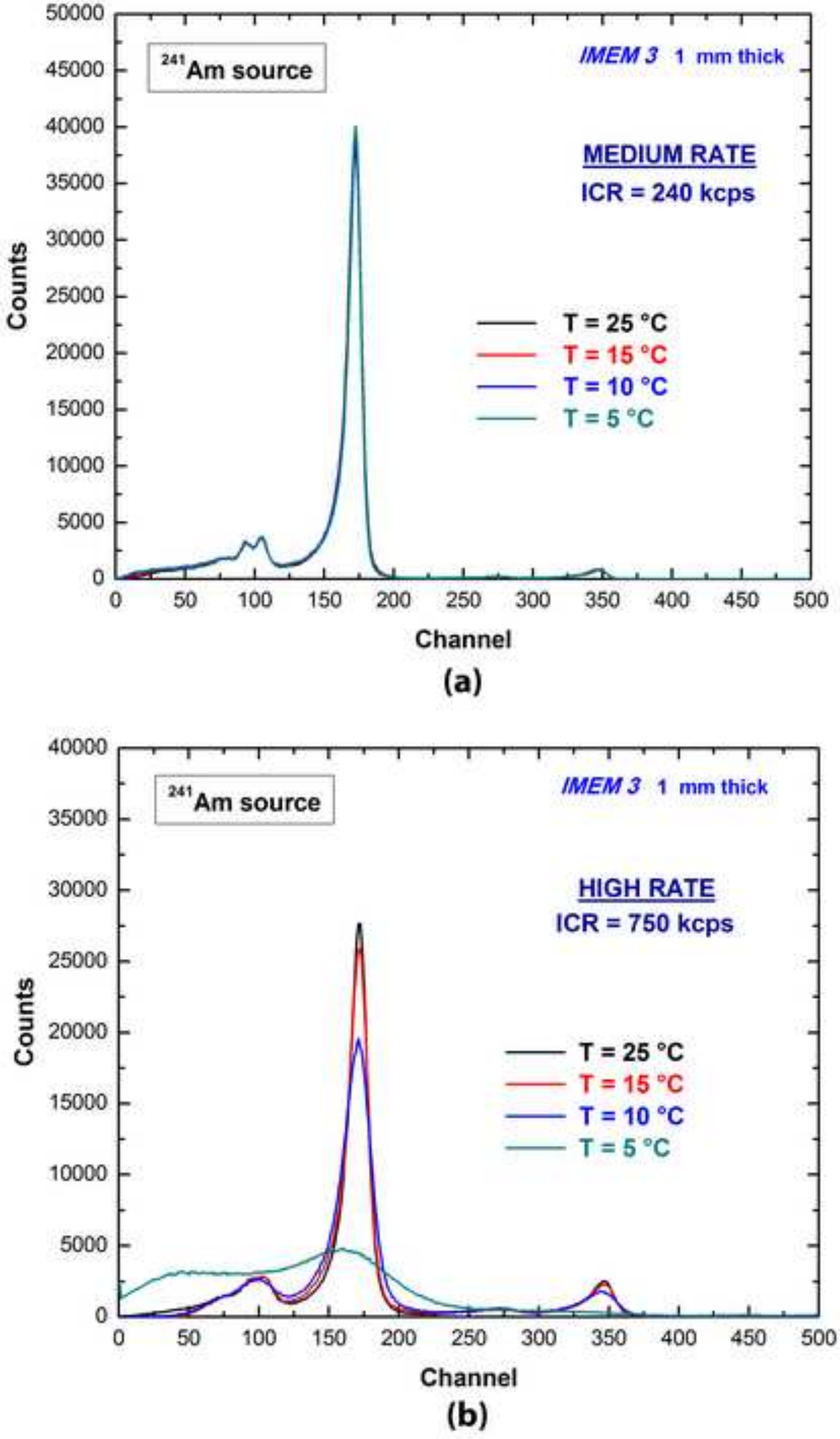

^{241}Am source
IMEM 3 1 mm thick
MEDIUM RATE
ICR = 240 kcps
T = 25 °C
T = 15 °C
T = 10 °C
T = 5 °C
Counts
0
5000
10000
15000
20000
25000
30000
35000
40000
45000
50000
Channel
0
50
100
150
200
250
300
350
400
450
500
(a)
^{241}Am source
IMEM 3 1 mm thick
HIGH RATE
ICR = 750 kcps
T = 25 °C
T = 15 °C
T = 10 °C
T = 5 °C
Counts
0
5000
10000
15000
20000
25000
30000
35000
40000
Channel
0
50
100
150
200
250
300
350
400
450
500
(b)

Figure 21

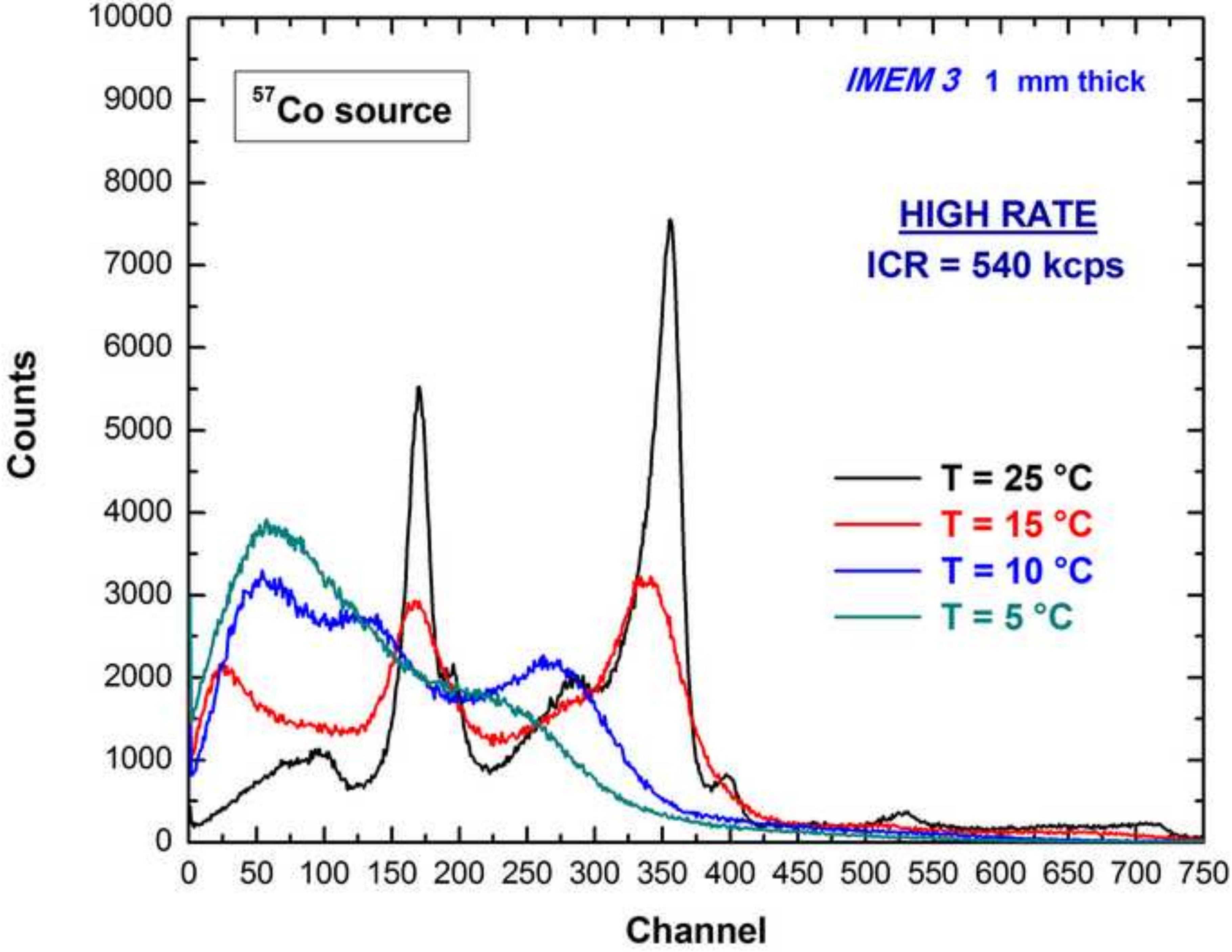

57Co source
IMEM 3 1 mm thick
HIGH RATE
ICR = 540 kcps
T = 25 °C
T = 15 °C
T = 10 °C
T = 5 °C
Counts
Channel
0
1000
2000
3000
4000
5000
6000
7000
8000
9000
10000
0
50
100
150
200
250
300
350
400
450
500
550
600
650
700
750

Figure 22

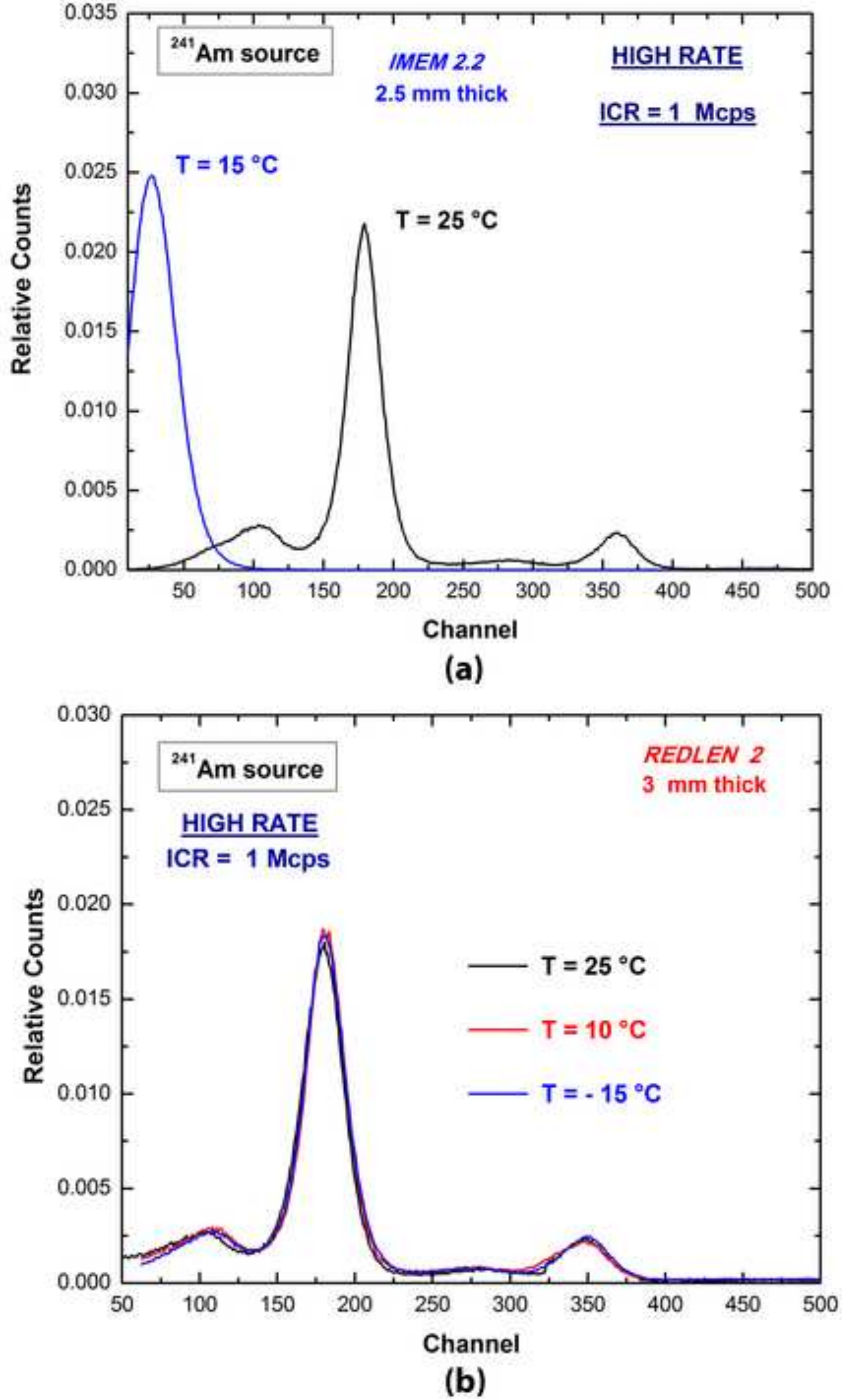

241Am source
IMEM 2.2
2.5 mm thick
HIGH RATE
ICR = 1 Mcps
T = 15 °C
T = 25 °C
Relative Counts
Channel
0.000
0.005
0.010
0.015
0.020
0.025
0.030
0.035
50
100
150
200
250
300
350
400
450
500
241Am source
REDLEN 2
3 mm thick
HIGH RATE
ICR = 1 Mcps
T = 25 °C
T = 10 °C
T = - 15 °C
Relative Counts
Channel
0.000
0.005
0.010
0.015
0.020
0.025
0.030
50
100
150
200
250
300
350
400
450
500

(a)

(b)

TABLE 1. CHARACTERISTICS OF THE SAMPLES.

Sample	Crystal Size (mm^3)	Growth Technique	Electrodes
IMEM 3	4.1 x 4.1 x 1	B-VB	Gold (Electroless)
REDLEN 2.1	4.1 x 4.1 x 1	THM	Gold (Electroless)
IMEM 2.2	4.1x 4.1 x 2.5	B-VB	Gold (Electroless)
REDLEN 2	4.1 x 4.1 x 3	THM	Gold (Electroless)

Table 2. LOW-RATE (200 CPS) SPECTROSCOPIC PERFORMANCE OF THE 1MM THICK B-VB GROWN CZT DETECTOR (IMEM 3).

	Energy (keV)		
	22.1	59.5	122.1
Energy resolution *FWHM* (%) at T = 25 ° C (bias voltage - 900 V)*	10	4.1	3.6
Energy resolution *FWHM* (%) at T = 5 ° C (bias voltage - 1100 V)*	8.0	3.8	3.4

*These results were obtained by using both the digital electronics, with a snapshot time *ST* of 9 µs, and a standard analog electronics: Gaussian shaping amplifier (shaping time constant of 1-2 µs) and a multichannel analyzer (MCA).

Table 3

Table 3. HIGH-RATE (UP TO 750 KCPS) SPECTROSCOPIC PERFORMANCE OF THE 1MM THICK B-VB GROWN CZT DETECTOR (IMEM 3) AT T = 25 °C.

	Energy and ICR	
	59.5 keV at 750 kcps	122.1 keV at 540 kcps
Energy resolution *FWHM* (%)*	8.7	5.7
Throughput (%)*	61	51

*These results were obtained by using the fast PSHA (dead time = 270 ns) and the PSD. The cathode bias voltage of the detector is equal to -1100 V.